MODELING OF COLD WELDING AND LAMINATION OF ORGANIC AND HYBRID ORGANIC /INORGANIC STRUCTURES

A THESIS SUBMITTED TO THE GRADUATE FACULTY IN PARTIAL FULFILMENT OF THE REQUIREMENTS FOR THE AWARD OF A MASTER OF SCIENCE DEGREE IN MATERIALS SCIENCE AND ENGINEERING

BY

ASUO, IVY MAWUSI

(MATERIALS SCIENCE AND ENGINEERING)

2011

Declaration

I hereby declare that this thesis entitled "Modeling of Cold Welding and Lamination of Organic and Hybrid Organic/Inorganic Structures" is the result of my research done under the supervision of Prof. Winston Oluwole Soboyejo at African University of Science and Technology, Abuja-Nigeria, and that no part of it has been presented for another degree in this University.

Asuo Ivy Mawusi

Date: 06 / 11 / 2011

(Student)

Prof. Winston O. Soboyejo

. . . . . Date . . . . . .

(Supervisor)

Dedication

This work is dedicated to my lovely mother, Miss Rogate Nfodjo and only brother Mr. Daniel Ewoenam Asuo.

Acknowledgements

He alone deserves all the glory, honour and adoration. All thanks to God for His protection, wisdom, understanding, and guidance throughout my duration of study in this institution. When all hopes were fading away, He still showed His steadfast love and mercy towards me.

I am also indebted to my mother, Ms. Rogate Nfodjo, Mr. Daniel E. Asuo and my other siblings for their love, prayers and sponsoring my education.

My sincere gratitude goes to my supervisor, Prof. Winston O. Soboyejo, for his encouragement, advice, guidance and time during my stay in AUST despite his busy schedule. It has been a great privilege to have him as my lecturer and supervisor.

Special thanks go to Prof. Osseo-Asare and all materials science faculty members for their advice, time and knowledge they have impacted in me. I also want to appreciate Prof. Douglas Buttrey, Prof. Tom Vogt, Dr. Joe Berry and Prof. T. DebRoy for the personal relationship I have with them and their advice. I say thank you to you all.

My sincere thanks go to Edmond N.Y. Doumon, my project partner and a good friend; you have been so helpful throughout this thesis work. Thank you for your support. My special gratitude to Mr. Daniel Kpeglo for his inspirations, prayers and supports; I really appreciate all you've done. To crown it all, I am so grateful to all my class mates: John, Shola, Emmanuel, Edward, Azeko, Vodah, Vitalis, Musah and Yiporo, it has been so lovely having you guys around.

Thank you all and God richly bless you…….

Table of Contents

Pages

List of Figures

Figures **Pages**

Figures **Pages**

Figures **Pages**

Abstract

This research work presents the results of analytical studies of effects of pressure and adhesion energy on the interfacial properties of cold welded and laminated surfaces in organic and Hybrid Organic/Inorganic electronic structures. The analytical modeling is based on the physics of elastic behaviour of a cantilever beam. The energy balance approach was employed to model the surface contacts in Hybrid Organic/Inorganic structures, HOISOLs, and Organic Light Emitting Diodes, OLEDs. The results show that pressure can be used to alter the morphology and adhesive energies of cold-welded and laminated organic and hybrid electronic devices. This model also provides new insights into how the presence of Titanium dioxide nanoparticles affects the adhesion and contact profile of layered HOISOLs electronic structures.

CHAPTER ONE

1.0. Background and Introduction

Energy is an important feature in life, and it is needed for applications in the industries, agriculture, transport services and other applications. Energy ranks the top societal need for the past five decades.[1] Eventually, clean, renewable energy including solar energy, wind energy and fossil fuel becomes a prime issue. A promising candidate among these renewable energy technologies is solar energy. This is because the sun is an abundant resource on earth. In every minute, the sunlight that reaches the earth's surface is enough to meet the world's energy demand for a whole year.[2] Solar energy provides clean electricity from photovoltaic panels for applications in industry, business centres, and homes to replace power generated by coal, oil and nuclear plants.[2] Since the use of these forms of energy results in serious air pollution, waste, damming of rivers, and environmental drawbacks, such as global warming, which is related to emission of carbon dioxide, CO_2 [1], there is a need to explore alternative energy approaches, such as solar energy.

Some of the advantages of solar cells include: their potential for long term applications (up to 35 years) in on-grid and off-grid areas; their lack of emissions, and their relatively low maintenance costs, which is associated with their lack of moving parts.

The sun is the earth's nearest star and the source of virtually all the Earth's energy. It produces ~ 3.8 $x10^{23}$ kW of power via nuclear fusion reactions. Our planet receives about 1.2×10^{17} W of solar power, while the worldwide energy consumption is about 10,000 times smaller at

1.3×10^{13}W. This means that the earth receives more solar energy in an hour than the total energy it consumes in an entire year.[2]

The energy we derive from coal, petroleum, paraffin, hydroelectricity and our food originates indirectly from the sun. Energy can be collected from the sun directly for heating, drying, distilling and generating electricity. Solar energy arrives at the edge of the earth's atmosphere at the rate of about 1350 W/m^2. This is referred to as the solar constant. However, not all energy reaches the earth's surface, because the atmosphere absorbs and reflects much of it. Also, the time the solar energy reaches the earth's surface, it is reduced to a maximum of about 1000 W/m^2 in tropical countries.[2]

1.1 Introduction To Hybrid Organic/Inorganic Electronic Structures

Since the breakthrough in discovering organic electroluminescence by Tang and Vanslyke in 1987 [4] and by Friend et al. in 1990, [3] describing Organic Light Emitting Diodes (OLEDs) based on small molecular weight or polymerized organic structures, intensive academic research and substantial commercial efforts have led to improved understanding of materials and device structures. One of today's dominant uses of Organic semiconductors is in emissive display technologies.

In an effort to improve the optoelectronic properties of organic electronic structures, inorganic materials have been doped into the organic layers within OLEDs.[12] Such doping has also been suggested as a way of improving charge transport in hybrid organic-inorganic light emitting

devices in which charge recombination can occur before electron-hole pairs reach the electrodes.[12]

Over the past few decades, conventional solar cells have been made from inorganic materials such as silicon.[5] Even though they have high module efficiencies between 20% - 24%, they are very expensive ($2-3 /watts), compared to the wages of $1-2 /day in the developing world.[5] This has stimulated increasing interest in the production of efficient and less expensive organic solar cells and hybrid organic/inorganic electronic devices.

Organic electronic structures use organic materials in the active layer of the devices. They offer several advantages such as lightness, mechanical flexibility, low production costs, and ease of processing. They also have a high potential for large area solar conversion.[6] However, their relatively low energy conversion still remains a major obstacle to their application.

One approach that can be used to improve the energy conversion of organic devices is to mix inorganic semi-conducting materials with the organic semi-conductors in hybrid organic/inorganic structure. Such inorganic semi-conductors can promote charge diffusion, while reducing the charge recombination that gives rise to reduced efficiencies in organic solar cells. The hybrid organic/inorganic structure can also be tailored to promote high adsorption and charge hopping in the active layer.[7] However, there have been only limited studies of adhesion and charge transport in hybrid organic/inorganic solar cells (HOISOLs) [11] and hybrid organic/inorganic light emitting diodes (HOILEDs).[3][11]

Furthermore, although the important of charge transport between the layers of HOISOLs and HOILEDs is well recognized [11], there have been few prior studies [13] of adhesion and surface contacts in HOISOLs and OLEDs. Such studies are needed because the adhesive energies between the individual layers affects charge transport through partially de-bonded layers. Relatively high current densities in areas of partial contact could also lead to increased localized heating, oxidation, and interfacial reactions that can affect the overall device performance.[13]

Prior work on HOISOLs has been reviewed by McGhee,[11] These shows that, several electron acceptors have been used to fabricate efficient devices. They include: conjugated polymer,[15] fullerenes,[16] and inorganic nanocrystals.[17] For the inorganic acceptors, the most studied materials include metal oxides, such as zinc oxide and titanium dioxide. [6]

In the case of TiO_2, HOISOLs have been produced with TiO_2 nanoparticles, porous networks, and also via the formation of titanium dioxide from a precursor. [9] These have shown that TiO_2 morphology and volume fraction affects: light absorption, exciton diffusion, and forward electron transfer, and charge transport. However, undesirable recombination processes, such as duplicate recombination and back electron transfer, should be limited. [9] There is, therefore, the need to obtain materials with improved adhesion and surface contact.

1.2 Problem Description

The properties, performance and lifetime of hybrid electronic devices depend on the properties of the active layer and the interfaces between the layers. However, so far, most research efforts have focused on improving efficiency and charge transport in the active layer. This has been achieved

largely by replacing PCBM (1-(3 methoxycarbonyl) propyl-1-phenyl [6,6]C61) layer with TiO_2. In this work, a theoretical approach is used to model the contact between layers that are relevant to hybrid organic/inorganic electronic devices with TiO_2 inorganic nanoparticles. The focus will be on modeling of cold welding and lamination of organic and hybrid organic/inorganic structures. The models will explore the improvements in contact that can be achieved through the application of pressure during the lamination of hybrid organic/inorganic solar cells (HOISOLs).

1.3 Structural Overview

These hybrid organic/inorganic electronic devices are based on the common ITO/PEDOT:PSS/P3HT:PCBM/LiF/Al structure that has led to some of the highest-reported efficiencies for OPV cells to date.[8] By replacing the PCBM with ordered TiO_2 nanostructures charge transport within the active layer can be modified. The modification can be controlled by varying the TiO_2 volume fraction, particle size, as shown in Figure 1.0.

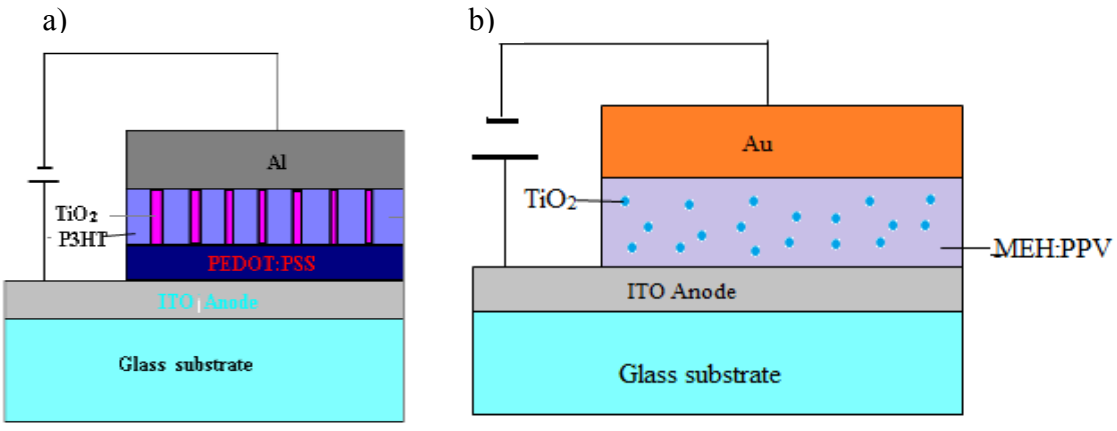

Figure 1.0 Structures of (a) HOISOL and (b) HOILED

1.4 Scope of Work

This project will explore the effects of TiO_2 nanoparticles on the adhesion and contact of HOILEDs and HOISOLs. The effects of lamination pressure will also be explored by analytical modeling. This work will be carried out in the following steps:

i. Review of relevant literature on OLEDS, HOISOLs, adhesion and contacts in organic and hybrid organic/inorganic electronic structures.

ii. Examine the combined effects of adhesion and lamination on the cold welding of OLEDs/HOILEDs.

iii. Modeling of contact due to lamination between layers with / without considerations of adhesion between layers that are relevant to HOISOLs and HOILEDs.

CHAPTER TWO

2.1 Overview of Photovoltaics

Historically, the photovoltaic effect, i.e. light- induced voltage was first discovered in 1839 by E. Becquerel when he incident light onto a silver chloride electrode in an electrolyte solution.[18] Charles Fritts also demonstrated the first solid-state solar cell in 1883 by depositing a thin layer of gold on selenium semiconductor.[18] The semiconductor served as the light absorber to convert photons into electron-hole pair, and the internal electric field in the Au/Se Schottky junction separated the photo-excited charge carriers. The device efficiency was only around 1%. [21] The two fundamental processes, namely light absorption and charge separation, are still the basis in all inorganic solar cells today. Modern solar cells was patented by Russell Ohl in 1946 [19] and demonstrated in 1954 by Chapin, Fuller and Pearson at Bell Laboratories. [22] Their cell employed a single-crystal Si (sc-Si) wafer for light absorption and p-n junction for charge separation, with an efficiency of 6%. [22]

Presently, solar cells comprising inorganic and organic semiconductors, such as mono-and multi-crystalline silicon, have found markets for small scale devices such as solar panels of roofs, pocket calculator and water pumps. These conventional solar cells can harvest as much as 24% of the incoming solar energy. [23]

Today, the production of these solar cells still requires many energy intensive processes at high temperatures (400 – 1400^0C) and high vacuum conditions, with numerous lithographic steps, leading to relatively high manufacturing costs.[24]

There is, therefore, a need to explore ways of reducing the manufacturing costs. This may be achieved through novel processing e.g. via the processing of thin films on substrates, and the use of alternative materials such as GaAs, $CuInSe_2$, $CuInGaSe_2$, ZnO_2, TiO_2 and organic materials.

2.2 Electronic Structure and Semiconductors

In semiconductors the primary interest is in the valence band and conduction band.[26] Moreover, in most applications the interest lies in what happens near the top of the valence band and the bottom of the conduction band. These states originate from the atomic levels of the valence shell in the elements making up the semiconductor.

The principles of semiconductor are usually illustrated by the example of silicon, a group four elemental semiconductor. The silicon crystal forms the so-called diamond lattice, where each has four nearest neighbours at the vertices of a tetrahedron. The four-fold tetrahedral coordination is the result of the bonding arrangement, which uses the four outer (valence) electrons of each silicon atom.[25] Each bond contains two electrons and all the valence electrons are taken up by the bonds.

According to quantum theory, the energy of an electron in the crystal must fall within well-defined bands. The energies of the valence orbital; which forms bond between the atoms represents band of states, the valence band. The next higher band is the conduction band which is separated from the valence band by the energy gap or band gap. The width of the band gap E_c - E_v is very important characteristic of the semiconductor and is usually denoted by Eg.[22]

The energy gap, *Eg*, and its structure as a function of the wave vector are key characteristics of semiconductor materials. They are of fundamental importance to the operation of solar cells. The principal features of interest are the temperature variation of the energy gap, *Eg*, and the magnitude of wave vector associated with low-energy transitions. The variation of the band gap with temperature can also be associated with low energy transitions. The variation of the band gap with temperature can be described by the following expression [26]:

$$E_g(T) = E_{g0} - \frac{\alpha T^2}{T + \beta} \qquad \textbf{(2.10)}$$

where T is the absolute temperature and the parameters α and β have their corresponding values. The current produced by solar cells is generated by optical transition across the band gap. Two types of such transitions can be distinguished: direct transition where the momentum, P given by:

$$P = \frac{E}{c} = \hbar k \qquad \textbf{(2.11)}$$

where c is the velocity of light, of the resulting electron-hole pair is very close to zero and indirect transition, k is the wave-vector, and the resulting electron hole pair has a finite momentum. An optical photon has energy of the order of 10^{-19} J and, since $c = 3 \times 10^8$ ms^{-1}. The second type of transition requires the assistance of a phonon (quantum of lattice vibration). Thus, there are two types of semiconductors: direct and indirect gap.[26]

2.2.1 Direct and Indirect gap Semiconductor

The band gap represents the minimum energy difference between the top of the valence band and the bottom of the conduction band. However, the top of the valence band and the bottom of the conduction band are not generally at the same value of the electron momentum. In a **direct band gap semiconductor**, the top of the valence band and the bottom of the conduction band occur at the same value of momentum, as in the schematic below.

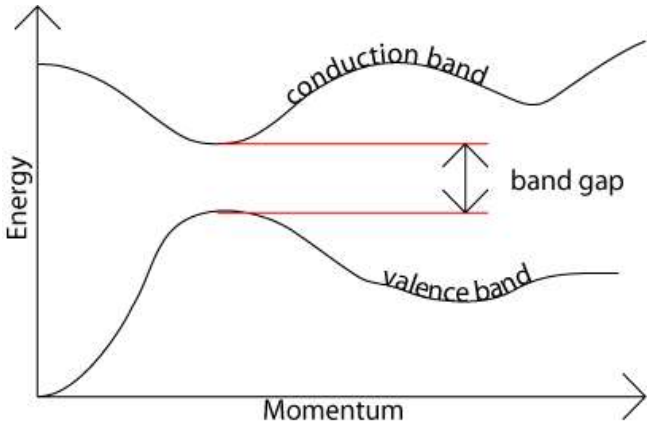

Figure 2.1(a) Illutration of direct band gap semiconductor

In an **indirect band gap semiconductor,** the maximum energy of the valence band occurs at a different value of momentum to the minimum in the conduction band energy:

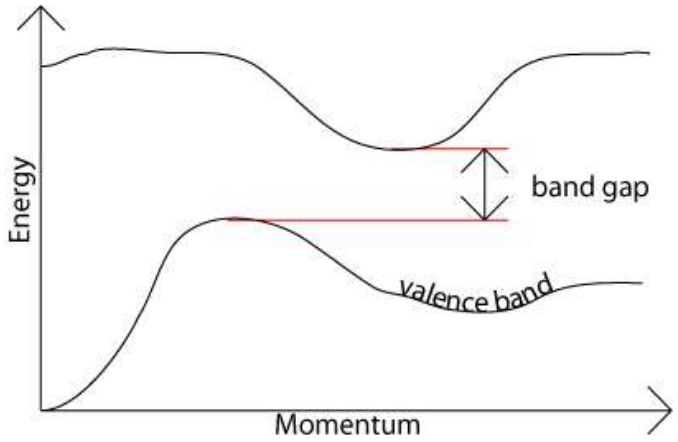

Figure 2.1(b) Illustration of indirect band gap semiconductor

The difference between the two gaps is most important in optical devices. As mentioned earlier, a photon can provide the energy to produce an electron-hole pair.

A photon of energy, E_g, can produce an electron-hole pair in a direct band gap semiconductor quite easily. This is because the electron does not need to be given very much momentum. However, an electron must also undergo a significant change in its momentum, for a photon of energy E_g, to produce an electron-hole pair in an indirect band gap semiconductor. This is possible, but it requires such an electron to interact not only with the photon to gain energy, but also with a lattice vibration called a phonon in order to either gain or lose momentum. [11]

The indirect process proceeds at a much slower rate, as it requires three entities to intersect in order to proceed: an electron, a photon and a phonon. This is analogous to chemical reactions, where, in a particular reaction step, a reaction between two molecules will proceed at a much greater rate than a process which involves three molecules. [28]

The same principle applies to recombination of electrons and holes to produce photons. The recombination process is much more efficient for a direct band gap semiconductor than for an indirect band gap semiconductor, where the process must be mediated by a phonon.

As a result of such considerations, gallium arsenide and other direct band gap semiconductors are used to make optical devices such as light emitting diodes, LEDs, and semiconductor lasers, whereas silicon, which is an indirect band gap semiconductor, is not. [28] Below is a plot showing the band gap and lattice constants of some semiconducting materials.

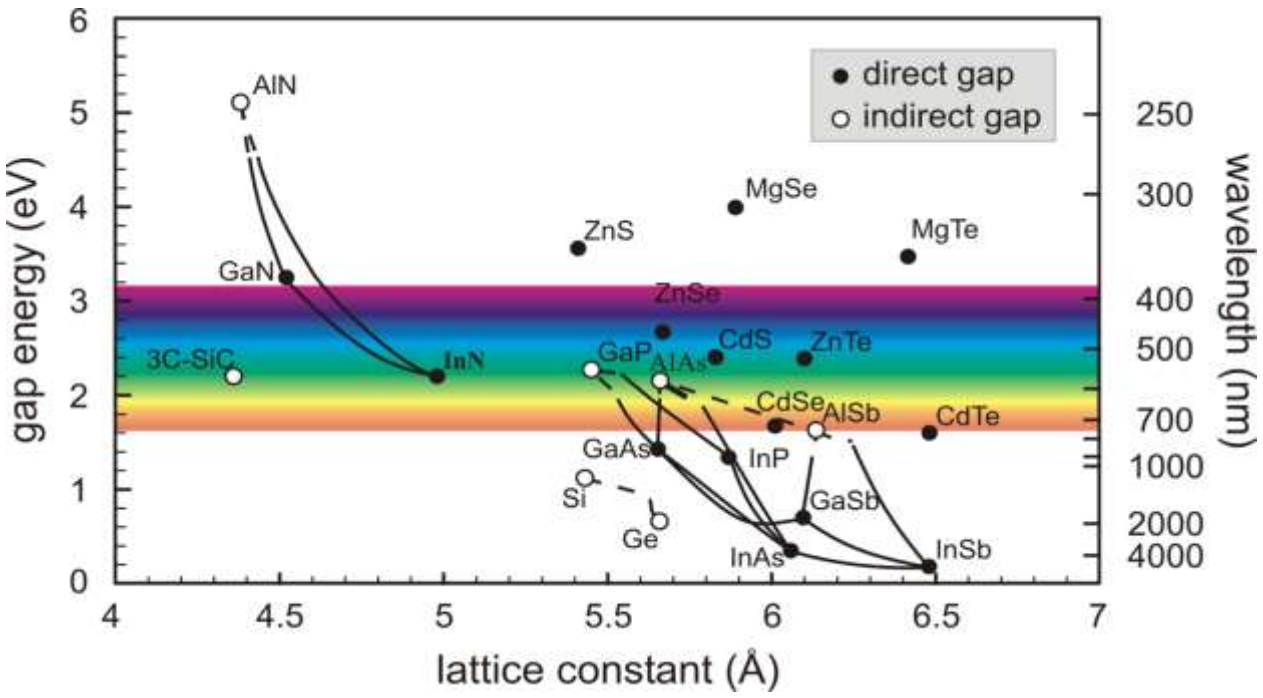

Figure 2.11 Band gap and lattice constants of semiconducting materials

2.2.2 Electrical Characteristics of Solar Cell

Electrically, the solar cell is equivalent to a current generator in parallel with an asymmetric, non-linear resistive element i.e. a diode, as shown in the equivalent circuit of Figure 2.12. The corresponding I-V curve is shown in Figure 2.13.

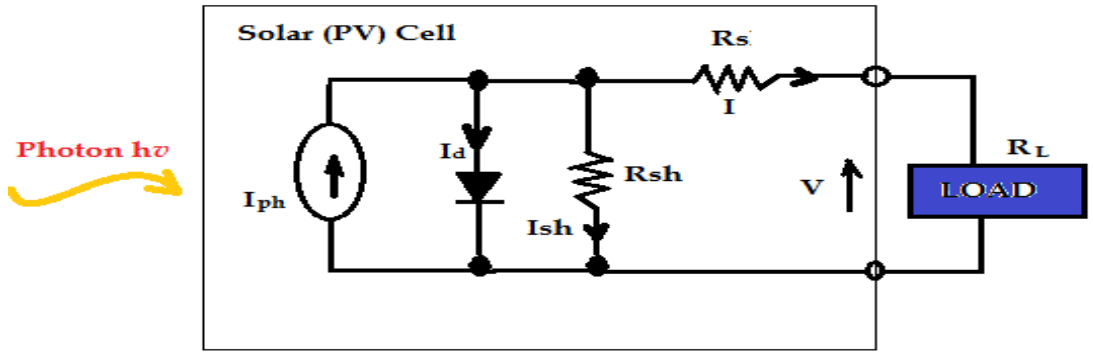

Figure2.12 Simplified equivalent circuit model for a photovoltaic cell

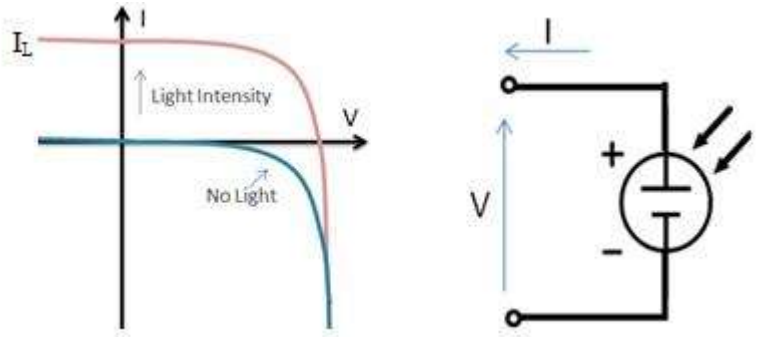

Figure 2.13 Current-voltage response of photovoltaic device under illumination

The corresponding I – V characteristic is described by the Shockley solar equation [26] given as:

$$I = I_{ph} - I_o\left(e^{\frac{qV}{k_B T}} - 1\right) \qquad \textbf{(2.12)}$$

where k_B is the Boltzmann constant, T is the absolute temperature, q (> 0) is the electron charge and V is the voltage at the terminal of the cell. I_o is known as the saturation current, which manifests that a solar cell in the dark is simply a diode. The photogenerated current I_{ph} is usually independent of the applied voltage, with possible exceptions, in the case of silicon and some other thin film materials. [31]

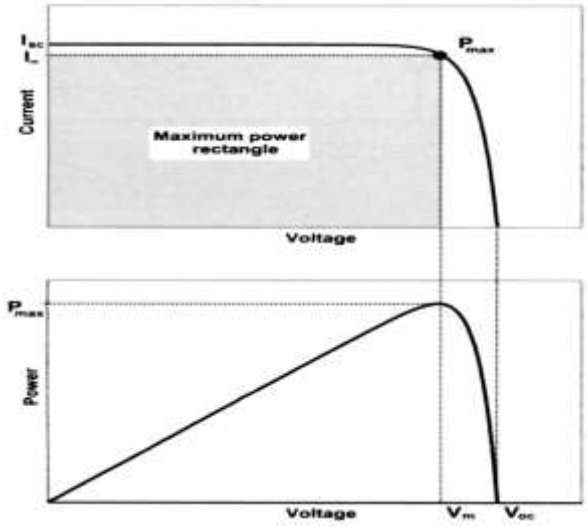

Figure 2.14 The I-V characteristic of an ideal solar cell (a) and the power produced by the cell (b) the power generated at the maximum power point is equal to the shaded rectangle in (a)

Figure 2.14(a) shows the I-V characteristic (Equation (2.12)). In the ideal case, the short circuit current I_{sc} is equal to the photogenerated current I_{ph}, and the open circuit voltage V_{oc} is given by:

$$V_{oc} = \frac{k_B T}{q} \ln\left(1 + \frac{I_{ph}}{I_o}\right) \qquad \textbf{(2.13)}$$

2.2.3 Efficiency of Solar Cell

The maximum theoretically achievable values of the short circuit current density I_{sc} and V_{oc} of the open circuit voltage can be obtained for different materials. The power $\boldsymbol{P = I_{sc}V_{oc}}$ produced by the cell depends on the load resistance and can be determined graphically as shown in Figure 2.14(b). The cell generates the maximum power P_{max} at a voltage V_m and current I_m. The fill factor, *FF*, of a device is defined as the ratio between the maximum power delivered to an external circuit and the potential power [26] given as :

$$FF = \frac{I_m V_m}{I_{sc} V_{oc}} = \frac{P_{\max}}{I_{sc} V_{oc}} \qquad \textbf{(2.14)}$$

The efficiency $\boldsymbol{\eta}$ of the cell is the power density delivered at operating point as a fraction of the incident light power density, P_s [29] given as:

$$\eta = \frac{I_m V_m}{P_s} \qquad \textbf{(2.15)}$$

The solar efficiency is also related to I_{sc} and V_{oc} using *FF* in the expression below:

$$\eta = \frac{I_{sc} V_{oc} FF}{P_s} \qquad \textbf{(2.16)}$$

The four quantities: I_{sc},V_{oc}, FF and η are the key performance characteristics of a solar cell. The Standard Test Condition (STC) for solar cells is the Air Mass 1.5 spectrum, an incident power density of 1000 Wm^{-2}, and a temperature of 25 ^{o}C.[19]

2.2.4 Quantum Efficiency

The photocurrent generated by a solar cell under illumination at short-circuit is dependent on the incident light. To relate the photocurrent density, I_{ph}, to the incident spectrum we need the cells quantum efficiency (QE). The quantum efficiency of a solar cell is defined as the ratio of the number of electrons in the external circuit produced by an incident photon of a given wavelength to the number of photons of a given energy. Thus, one can define external and internal quantum efficiency denoted by EQE(**λ**) and IQE(**λ**), respectively. [30]

The external quantum efficiency (EQE), also known as the incident photon conversion efficiency, is given by the number of electrons generated per incident photon**:**

$$EQE = \frac{n_e}{n_{ph}} = \frac{I_{sc}}{P_o}\frac{hc}{\lambda e} \qquad \textbf{(2.17)}$$

where n_e is the number of electrons, n_{ph} is the number of photons, I_{sc} is the short circuit current, P_o is the incident optical power, h is Planck's constant, c is the speed of light, λ is the wavelength of light, and e is the electrical charge.

This generally follows the absorption spectrum of the materials constituting the organic photovoltaic, OPV. The internal quantum efficiency is also known as the photocurrent action

spectrum, and it is given by the ratio of the photocurrent to the absorbed photon flux. Theoretically, we can calculate the power efficiency of a solar cell can by using a solar simulator that replicates the solar spectrum. The visible and near-infrared portions of the AM1.5 spectrum[31] are shown in Figure 2.15.

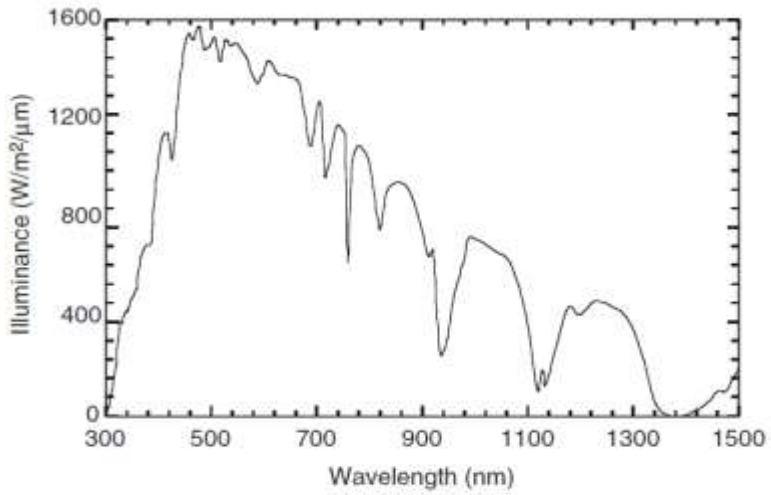

Figure 2.15 Solar irradiation spectrum for AM0 and AM1.5 illumination [31]

2.2.5 Light Absorption by a Semiconductor

The photovoltaic energy conversion relies on the quantum nature of light where the energy of light as a flux of particles- photons is defined by:

$$E_{ph}(\lambda) = \frac{hc}{\lambda} \qquad \textbf{(2.18)}$$

When a photon of light enters a semiconductor, it may be absorbed and excite an electron from the valence band to the conduction band and leaves a hole in the valence band; the absorption process generates electron-hole pairs. [22]

Each semiconductor is, therefore, restricted to converting only a part of the solar spectrum. The solar radiation spectrum for direct light at both the top of the earth's atmosphere and at sea level is shown in the diagram below in Figure 2.16.[22, 30]

The production of light from the sun is similar to the distribution of what would be expected from blackbody. In addition, light is redistributed by Rayleigh scattering, which is responsible for the blue colour of the atmosphere. As light passes through the atmosphere, some is absorbed by gases with specific absorption bands. The nature of the absorption process also indicates how a part of the incident photon energy is lost in the event. The excess energy is lost as heat and cannot be converted into useful power. This represents one of the fundamental loss mechanisms in a solar cell.

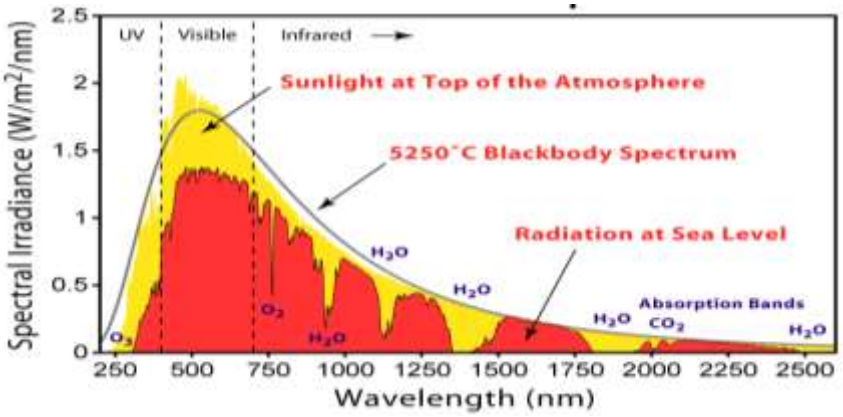

Figure 2.16 Solar radiation spectrums

2.3 Mobility of Charges in Semiconductor

Another important parameter of a semiconductor is the mobility μ or charge carrier drift velocity υ per unit field E. This is given by the expression:

$$\mu = |\upsilon| / E \qquad \textbf{(2.19)}$$

This parameter is defined as positive for both holes and electrons. The electrical conductivity $\boldsymbol{\sigma}$ is the sum of contributions from the concentrations of electrons $\boldsymbol{n}$ and of holes $\boldsymbol{p}$ in accordance with the expression [33]:

$$\sigma = \left(ne\mu_e + pe\mu_h \right) \qquad \textbf{(2.20)}$$

where $\boldsymbol{e}$ is the electronic charge, μ_e the mobility of electrons and μ_h that of the holes.

The mobility has weak power-law temperature dependence T^n, and the pronounced $\boldsymbol{T}$ dependence of the conductivity is due principally to the dependence of the electron and hole concentrations on the temperature. In doped semiconductors this generally arises mainly from Boltzmann factor $\exp\left(-E_i / k_{\mathbf{B}} T\right)$ associated with the ionization energies E_i of the donors or acceptors.

The thermal energy $k_B T = 0.026\, eV$ at room temperature (300 K) is often comparable to the ionization energies. In intrinsic or undoped semiconducting materials, the main contribution is from the exponential factor $\exp\left(-E_g / 2k_B T\right)$ in the following expression from the law of mass action[33]:

$$n_i = p_i = 2\left(\frac{k_B T}{2\pi\hbar^2} \right)^{3/2} \left(m_e m_h \right)^{3/4} \exp\left(-E_g / 2k_B T \right) \qquad \textbf{(2.21)}$$

Where the intrinsic concentrations of electrons $\boldsymbol{n_i}$ and of holes $\boldsymbol{p_i}$ are equal to each other because the thermal excitation of $\boldsymbol{n_i}$ electrons into the conduction band leaves behind the same number $\boldsymbol{p_i}$ of holes in the valence band, that is $\boldsymbol{n_i = p_i}$.[33]

It is observed that the expression contains the product $\boldsymbol{m_e m_h}$ of the effective masses $\boldsymbol{m_e}$ and $\boldsymbol{m_h}$ of the electrons and holes, respectively. These effective masses strongly influence the properties of exciton.[33]

2.3.1 Polaron in Semiconductors

The motion of electrons in an ionic crystal gives rise to another quasi particle. When an electron is moving in an ionic crystal, its surrounding medium will be polarized, with negative ions being repelled and positive ions attracted towards it. The polarized field thus produced, in turn, affects the motion of the electron itself. This moving electron with its accompanying polarized field is known as a polaron. A polaron is a charge carrier. [58] Two classes of polarons are generally identified. These are small and large polarons. In small polarons, the size of the polarons is comparable to the lattice constant, and the electron-phonon coupling is very strong. Large polarons have relatively weak coupling and large size, e.g. GaAs is 0.068, CdTe is 0.29, and KCl is 3.44.[58]

Moreover, this accompanying cloud of polarisation causes an increasing effective mass decreasing the mobility of these quasi particles. Due to the dimerization of the bond, conjugated systems exhibit neither pure covalent nor pure polar bonds.

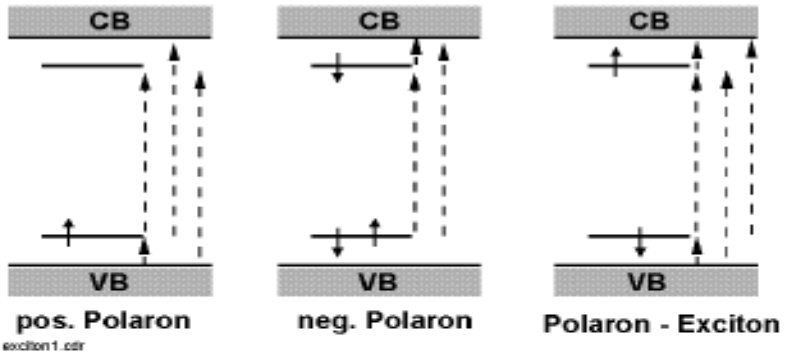

Figure 2.17 Energy levels of the positive and negative polarons as well as polaron-exciton

Arrows with solid lines represent electrons with spin orientation, arrows with dashed lines show possible intra gap transitions that can be used to detect and identify the excited species.

2.3.2 Exciton-Dissociation and Charge-Recombination Processes

Since the early days of organic electronics, quantum chemistry has proven to be a very valuable tool to understand the electronic and optical properties of the conjugated materials used in the devices. Quantum chemistry has also helped to define new strategies towards enhanced efficiencies. [37] Thus, the mechanisms governing the operation of organic-based devices, and in particular solar cells, can be adequately described at the quantum-chemical level. This is illustrated by focusing on two key processes in organic solar cells, namely the dissociation of photogenerated electron-hole pairs (which has to be maximized) and the germinate recombination of charge carriers at organic-organic interfaces.[37]

Recalling the working principle of organic solar cells; an organic solar cell is fabricated by sandwiching an organic later between two electrodes of different nature, typically indium tin oxide (ITO, which is metallic and transparent) and aluminum. This device is intended to convert light emitted by the sun in to electrical charges, which can then be collected by an external circuit.[38] For this to be accomplished, the photons initially penetrate into the organic layer through the transparent side of the device, and are absorbed by the organic material. The key aspect is then to have the photogenerated electron-hole pairs (excitons) dissociate into charge carriers. In general, the efficiency of the charge-generation process is extremely low if a single material is incorporated into the organic layer. This is explained by the fact that the binding energy of the exciton i.e., the strength of the Coulomb attraction between the electron and hole,

is significant in conjugated materials (it is generally considered to be around 0.3-0.4 eV in conjugated polymers and even larger in small molecules), [39] thus making excitons very stable species. Hence, the current organic devices rely either on multi-layered structures or blends made from an electron-donor component and an electron-acceptor component illustrated in Figure 2.23. The two components can be polymers (for instance, phenylenevinylene chain (PPV) with different substituents, [41] two different molecules, or a mixture of polymer and molecule (for instance, a conjugated polymer as the donor and C_{60} as the acceptor.[41] In such organic blends, the photons are absorbed by the donor or the acceptor, or by both.

If the donor absorbs most of the incident light, electron-hole pairs are generated on the donor moieties following the promotion of a pi-electron from their highest occupied molecular orbital (HOMO) level to their lowest unoccupied molecular orbital (LUMO) level. In order to dissociate into charge carriers, the excitons have then to migrate towards a donor-acceptor interface. This points to the predominant role of the morphology of the blends in defining the efficiency of the exciton-dissociation process. If each of the two components are deposited in separate layers, only the excitons that are generated close to the interface or that can reach it during their lifetime are likely to be converted into electrical charges; since the exciton diffusion range is generally limited in organic thin films to be in the order of 10 nm [42], such a double- layer structure is far from optimal. A largely distribute contact area between the two partners is thus required for efficient devices. This can be promoted by the homogeneous mixing of two components or by vertical segregation of the phases.[43]

The key role played by the morphology of the blends is further attested to by the fact that the efficiency of solar-cells can be improved by a postproduction treatment of the devices. [44] Once

an exciton reaches the donor-acceptor interface, the electron promoted in the LUMO level of the excited donor can be transferred to the lower-lying LUMO level of the acceptor, as illustrated in Figure 2.18 below**.**

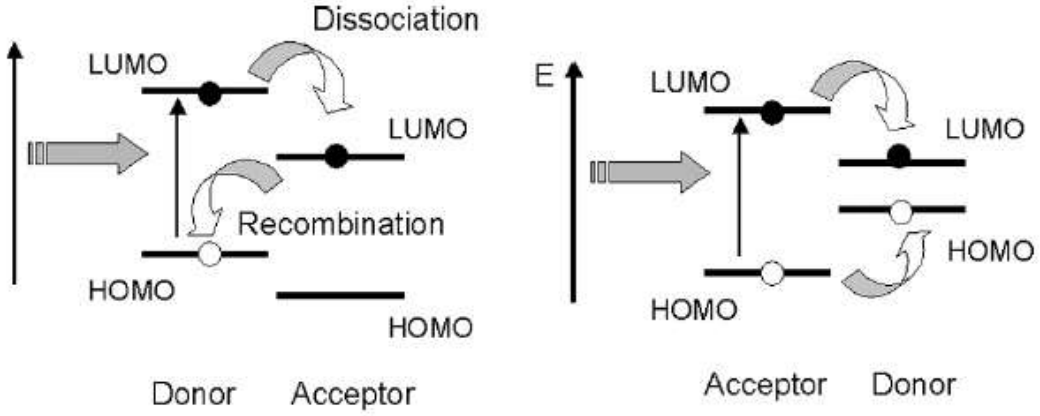

Figure 2.18 Illustration of the exciton-dissociation and charge-recombination processes (left) and of energy transfer (right) in a donor-acceptor pair [43]

If the hole then remains on the HOMO level of the donor, light is converted by this photoinduced electron-transfer process into electrical charges (i.e., one negative polaron on the acceptor and one positive polaron on the donor after the fast nuclear relaxation upon charge formation has occurred). But then, the same final charge-separated state can be reached when the acceptor is initially photoexcited, following a photoinduced hole-transfer from the HOMO level of the acceptor to the HOMO level of the donor.[31] Finally, the charge has to escape from mutual Coulomb attraction before migration towards the electrodes can occur, typically via a hopping mechanism, and possibly with the help of the built-in potential created by connecting the two different metallic electrodes.

2.4. Organic Semiconductors

From the past three decades, organic semiconductors have become very promising class of materials with present and potential applications in various optoelectronic devices. These organic materials are simpler to manufacture and have low production costs, thereby making them relative cheaper materials used in solar cells applications than inorganic semiconductors. Until recently, however, the power conversion efficiency of organic photovoltaic devices (OPVs) remained below 1% while the performance of organic light emitting diodes (OLEDs) has remarkably improved over the past 15 years. [30] However, the performance of solid state organic solar cells has increased significantly in the last 10 years,[30] with power conversion efficiencies under white light illumination (AM 1.5) greater than 8% for the best molecular, polymer and organic-inorganic hybrid solar cell. Polymeric materials used in solar cells are lightweight and they are inexpensive to fabricate but they only offer one-third of efficiency of inorganic materials. [30]

The types of material and fabrication methods are used to differentiate between polymer and molecular photovoltaics. Fabrication method whereby sublimation under vacuum of successive layers of electron and hole transporting materials are employed is used to fabricate molecular devices. The organic heterojunction is where charge photogeneration occurs at the interface between the two layers. [34]

In contrast, polymer OPVs are generally prepared by solution processing. The most efficient devices consist of blend of a conjugated polymer and a molecular sensitizer, or blends of two different conjugated polymers. Such blends have interfaces throughout the active layer, known as a bulk heterojunctions. [30]

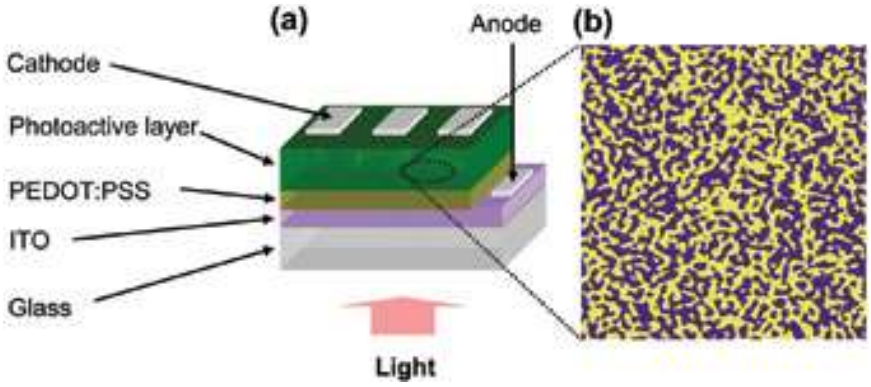

Figure 2.19 A typical solar cell structure and its topographic image

Figure 2.19 (a) shows a typical solar cell structure consisting of PEDOT:PSS deposited onto a glass/ITO substrate. The photoactive layer is spin -cast on top of PEDOT:PSS film, followed by the aluminum cathode electrode evaporation. (b) Topographic image obtained using atomic force microscopy showing phase separation where yellow and purple areas are donor and acceptor phases, respectively

2.4.1 History of Organic Photovoltaics

In 1986, Tang fabricated the first organic cells using phthalocyanine, CuPc, and perylene dimmide. He achieved a reasonable power conversion efficiencies of about 1% under AM 1.5 G light source by forming a bilayer through a vacuum deposition of CuPc and perylene dimmide based p-type and n-type organic semiconductor material between ITO transparent electrode and Al cathode.[30]

After about 20 years, there has been improvements through organic semiconductor's p-n junction this has results in substantial increase in the photoelectric conversion efficiency to about 8%.

The organic solar cell is divided into two, based on the different methods of manufacturing process which are vacuum deposition based device and solution process based device. [34]

The first vacuum deposition based device modified was in OLEDs. However the solution process based organic solar cells have better properties since there is formation a bulk heterojunction between a donor and acceptor. Therefore low cost and large-area displays can be produced using printing processes. The improvement steps of bulk heterojunction organic solar cell using a polymer donor, which enables low-cost production through solution process, and a PCBM, 1-(3-Methoxycarbonyl)-propyl-1-phenyl- (6,6)C61, based acceptor over the years are summarised in Figure 2.20 below:[35]

- **2003 – P3HT:PCBM(1:4), η=0.2%, not annealing**
  J.C. Hummelen *et al*, *Synthetic Metal*, **2003**, *138*, 299
- **2003 – P3HT:PCBM (1:1), η=3.5%, 75°C for 4min annealing**
  F. Padingger *et al*, *Adv. Funct. Mater.*, **2003**, *13*, 85
- **2004 – P3HT:PCBM (1:1), η=5%,** Christoph J. Brabec (SIEMENS)
- **2005 – P3HT:PCBM (1:0.6), h=5.2%, 155°C for 3min annealing**
  Marisol Reyes-Reyes *et al*, *Org. Lett.*, **2005**, *7*, 5749
- **2005 – P3HT:PCBM (1:0.8), η=4.9%, 155°C for 5min annealing**
  K. Kim *et al*, *App. Phys. Lett.*, **2005**, *87, 083506*
- **2006 – P3HT:PCBM (1:1), η=4.4%, 140°C for 120min annealing**
  Y. Kim *et al*, *Nature Mater.*, **2006**, *5*, 197
- **2006 – P3HT:PCBM (1:1), η=5%, Ca-Ag electrode/xylene solution casting**
  P. Schilinsky *et al*, *Adv. Funct. Mater.*, **2006**, *16*, 1669
- **2006 – P3HT:PCBM (1:0.8), η=5%, TiOx optical spacer**
  K. Lee *et al*, *Adv. Mater.*, **2006**, *18*, 572
- **2007 – PCPDTBT:$PC_{71}BM$ (1:2), η=5.5%, dithiol treatment**
  G.C. Bazan *et al*, *Nature Mater.*, **2007**, *6*, 1
- **2007 – P3HT:PCBM (1:0.8)/PCPDTBT:PC71BM, η>6%, TiOx optical spacer, Tandem**
  K. Lee *et al*, *Science*, **2007**, *317*, 222
- **2008 – P3HT:New Acceptor, η>5.98%, Plextronics**
- **2008 – New Low bandgap donors, η>6.23%, Konarka**
- **2009 – New Low bandgap donor, η>6%, K.Lee, Y.Yang, Y. Lian etc.**
- **2009 – New Low bandgap donor, η~7.9%, Solarmer**

Figure 2.20 Efficiency improvement status of organic solar cell unit device (KRICT, 2009) [35]

In 2003, the Hummelen Group reported photoelectric conversion efficiency of 0.2%, by combining P3HT, Poly (3-Hexylthiophene), with PCBM in the ratio 1:1. At the time PPV [poly(phenylenevinylene)] based materials were widely used. In that same year, the result was improved to 3.5% by the Padingger group, as they change the combination ratio of P3HT to PCBM to 1:1 and operated photoactive layer annealing at 75^{o} C for 4 minute. Eventually, various research groups such as those of C.J. Brabec, D.A. Carroll,Y. Yang, D.D.C. Bradley, G.C. Bazan and A.J. Heeger have enhanced the device efficiency through either heat treatment or solvent vaporization. As a result, over 5% efficiency was reported in 2008. Konarka in particular officially achieved an efficiency of 5.21% efficiency with 1.024 cm^2 a unit device, through an approved process that was conducted by NREL in 2006. This was achieved using P3HT:PCBM photoactive layer.[31, 34, 35]

In the last two years, Solarmer has announced its development of a unit device (aperture: 0.047 cm^2) with a 7.9% efficiency. This device also has a high fill factor of 70.87%**.** [35]

2.5 Hybrid Organic-Inorganic Photovoltaics

Organic solar cells use organic materials in the active layer of the devices. They offer several advantages such as lightness, mechanical flexibility, low production costs, and ease of processing. They also have a high potential for large area solar conversion.[31] However, their relatively low energy conversion still remains a major obstacle to their application. In recent years, this has stimulated increasing interest in the production of efficient and less expensive organic solar cells and hybrid organic/inorganic solar cells.

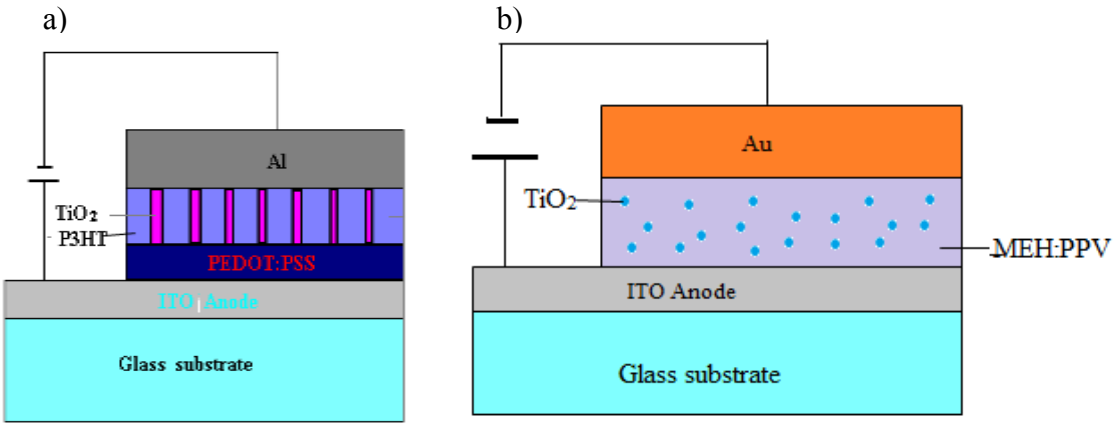

Figure 2.21 Structure of (a) HOISOL and (b) HOILED

Hybrid devices incorporating organic and inorganic materials are used due to the prospect of combining the advantages of both types of materials. One class of photovoltaic devices showing particular promise is based on composites of conjugated polymers and semiconducting nanocrystals, including quantum dots. Quantum dots are optical materials in which the crystal dimensions are reduced to the point where quantum confinement of excitations affects the electronic structure of the material.[31]

Quantum confinement leads to interesting effects, such as size-dependent optical gaps and novel nonlinear optical properties. High quality, monodisperse nanocrystals can be prepared by chemical means, [45] permitting the electronic structure to be tuned by varying the size of nanocrystals. Also, combining quantum dots with organic materials facilitate solution processing and device fabrication. [31] We also discuss the property of bulk heterojunction devices made from composite of conjugated polymers and TiO_2. Nanocrystalline TiO_2 has reasonably good electron transport properties. Its conduction band lies below the LUMO level of typical organic semiconductors.[31] Thus, TiO_2 is suitable to sensitize charge photogeneration. Bulk

heterojunction devices have been prepared by spin-coating the blends of conjugated polymers and TiO_2 nanocrystals, conversion of a TiO_2 precursor embedded in a polymer film, and infiltration of a conjugated polymer into a porous TiO_2 film. Multi-layered structures have also been tested in which a solid TiO_2 layer serves as the electron- transporting layer and charge photogeneration takes place at the organic- inorganic interface.

However, due to the intrinsic wide band gap of the TiO_2 materials (3 eV for rutile and 3.2 eV for anatase), both rutile and anatase absorbs ultraviolet light, which is typically around 5% of the spectral output of sunlight in the UV region while 45% is visible light.[31] In order to increase the spectral absorption of TiO_2 into the visible or even infrared region, it is extremely desirable to achieve significantly narrowed TiO_2 band gap, via band structure engineering by replacing some of the Ti atoms with other elements (alloying). This needs the identification of alloying elements that can stay in the TiO_2 sublattices to cause significant red-shift in the band gap.[31]

In 1991, Dye-Sensitized Solar Cells (DSSC; also known as Grätzel cells) attracted considerable attention since the report of 10% power conversion efficiency.**[46]** In these devices, TiO_2 nanoparticles are sensitized with a monolayer of a ruthenium-based dye. The nanoparticle film has a large surface area for dye absorption, resulting in efficient absorption of solar light. Charge transport occurs by hopping holes through a mesoporous titania structure and electrons through a liquid electrolyte has led to concern about device stability due to desorption of the dye, leakage of the electrolyte or corrosion of the electrode. These concerns have led a number of groups to explore devices in which an organic semiconductor film replaces the electrolyte.**[35]**

2.5.1 Polymer- Sensitized TiO_2

A number of groups have explored using titania (TiO_2) in organic-inorganic hybrid devices. TiO_2 has been used to fabricate highly efficient DSSCs and this has naturally led to investigation of bulk heterojunction devices using a conjugated polymer and TiO_2. Salafsky et al.[47] investigated charge photogeneration in films consisting of TiO_2 nanoparticles and PPV.[47, 48]

One way used to form polymer / TiO_2 bulk heterojunction that does not use nanocrystals involves preparing a composite film containing a conjugated polymer and a precursor to TiO_2.[49]

Polymer -TiO_2 composites were prepared by spin-casting a film containing MDMO-PPV (Poly(2-methoxy-5-(3'-7'-dimethyloctyloxy)-1,4-phenylenevinylene) and titanium (IV) isopropoxide [Ti $(OC_3H_7)_4$]. The TiO_2 precursor was then converted in the dark via hydrolysis in air to form a TiO_2 phase in the polymer film. The resulting film is insoluble and resistant to scratching. Based on X-rays photoelectron spectroscopy (XPS) measurements of the polymer-titania composite and a similarly prepared pure TiO_2 film, it was concluded that the TiO_2 conversion yield was at least 65%. Incorporation of TiO_2 into a polymer film quenched the photoluminescence, PL, intensity by nine-tenths at 25% TiO_2 (by volume). The photoinduced absorption spectrum of the MDMO-PPV- TiO_2 thin film shows peaks at 0.42 and 1.32 eV, consistent with polaron photogeneration, and the light-induced electron spin resonance, LESR signal is enhanced.[31]

Photovoltaic devices were prepared by sandwiching an MDMO-PPV/ TiO_2 composite between PEDOT:PSS, [Poly(3,4-ethylenedioxythiophene) poly(styrenesulfonate)] -coated ITO and LiF/Al electrodes. The photovoltaic properties of the device are shown in Figure 2.22 below

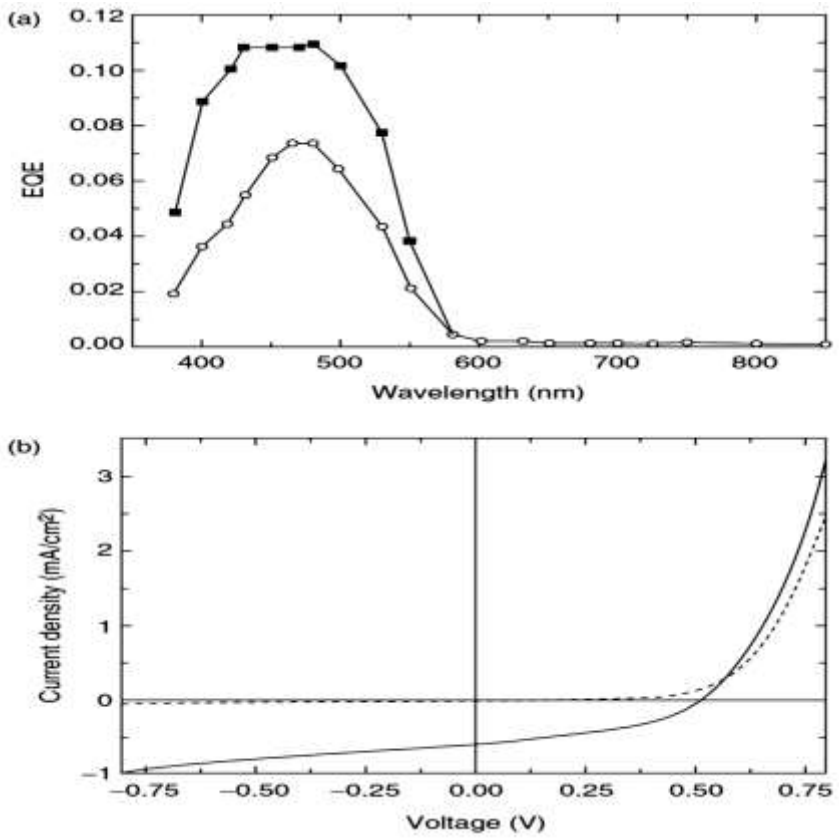

Figure 2.22 Photovoltaic properties of ITO/PEDOT:PSS/MDMO-PPV:TIO2/Li/Al device

In the figure, (a) is the plot of EQE vs. Wavelength of 1:1 (circles) and 4:1 (squares) blends by volume and (b) I-V characteristics in the dark (dashed line) and under ~70 mW/cm^2 illumination (solid line) of 4:1 device.

As shown in Figure 2.22, the peak EQE of 11% is reached between from 430 to 480 nm. The operating parameters of devices illuminated by a halogen lamp set at 0.7 sun intensity are I_{sc} = 0.6 mA/cm^2, V_{oc} = 0.52 V, and FF = 0.42. One interesting difference between this device and other bulk heterojunction device is that the peak EQE is reached at a loading of 20% by volume (roughly 40% by weight). This is much lower that peak EQE required for nanocrystals, suggesting that better dispersion of the sensitizer can be achieved via the precursor route that

spin-coating a composite film. The photocurrent is, however, much lower that obtain using other approaches.

2.6 Overview of Thin-film Deposition and Fabrication Techniques

It is desirable that organic electronic devices can be fabricated using a low-cost strategy, such as the roll-to-roll fabrication process. Two problems associated with this fabrication process are how to form the active-layer and the cathode mechanics and electronic contacts.[60] These may be partly overcome. Lamination techniques are attractive due to their simplicity and low cost. This technique has been reported to produce two layer heterojunction solar cells; however this technique is neither compatible with roll-to-roll fabrication process, nor applicable to bulk heterojunction solar cells.[60]

2.6.1 Electrodes and Active layer Materials

Transparent conductive oxides (TCO) have undergone significant commercialization and these films are commonly in applications, such as in digital watches, cell phones, computer screens or other types of displays. The most important TCO today is typically indium-tin-oxide (ITO), which has a chemical formula of In_2O_3:Sn. ITO is one of the few metalic oxides that combine many technologically interesting properties such as high transparency in the visible region of the solar spectrum, good electrical conductivity, and excellent substrate adherence. Organic optoelectronic device performance has been further enhanced by a variety of ITO surface treatment technologies, including the deposition of thin carbon layer, polyanilane and PEDOT by

oxygen plasma.[61] ITO on glass is used as a transparent electrode in nearly all flat panel displays (FPDs).

The cathode-organic interface, the hole injection efficiency from the ITO anode to the hole-transporting organic Layer is tuned through interface engineering and selecting organic molecules with energy alignment that favour ohmic injection from the ITO anode.[61]

Lee et al. [62] have recently shown that significant work function shifts can be obtained simply by dipping the ITO substrate in acid or base solutions. The resulting modifications to the device performance are also consistent with the work function shifts. Indium tin oxide (ITO) is used as the anode, while the cathode is usually a low work function metal such as aluminum although, Ca, Mg and Au are sometimes used. The top contacts of the aluminum electrode are applied using a thermal evaporator.

2.6.2 PEDOT:PSS

PEDOT is a relatively new member in the conducting polymer family. It shows interesting properties, including relatively good electrochemical, ambient, and thermal stability of its electrical properties, as compared with that of other polythiophenes. It is insoluble in many common solvents and unstable in its neutral state, as it oxidizes rapidly in air. To improve its processability, a polyelectrolyte solution (PSS) can be added. This results in an aqueous dispersion of PEDOT:PSS, where PEDOT is its oxidized state. This aqueous dispersion is deposited by spin-coating.

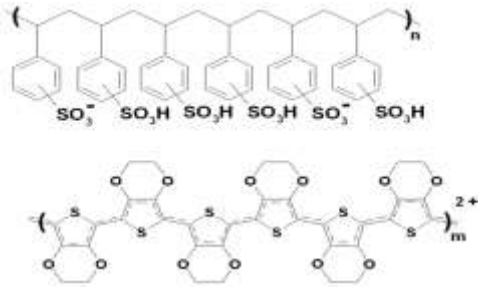

Figure 2.23 Molecular structure of PEDOT:PSS

2.6.3 P3HT:PCBM

The poly (3-hexylthiophene), P3HT and [6,6]-phenyl C_{61}-butyric acid methyester, PCBM, blends are some of the promising organic solar materials. They are the most efficient fullerene derivate based donor-acceptor copolymers so far.[63] Organic solar cells made from P3HT:PCBM active layers have been reported to have efficiencies between 5% and 8%.[63] Their structures are shown in Figure 2.24. PCBM is a fullerene derivative. Due to its high hole mobility, it plays the role of electron acceptor in many organic cells. In organic PV cells, we create a bulk heterojunction blend with PCBM (fullerene acceptor) and spin cast the mixture directly onto the device.

P3HT is among the polythiophene family. It is a conducting polymer. It is the excitation of the π-orbit electrons in P3HT that gives the photovoltaic effect in the blend. This polymer acts as a donor and facilitates exciton generation from light absorption in the material. However, with the presence of the delicate TiO_2 columns, other techniques will need to be used to deposit the P3HT evenly throughout the layer. Approximately 200 nm thickness is recommended in order to optimize light absorption. Some potential solutions include electropolymerization, reversing the structure such that the P3HT forms cylinders in porous TiO_2, and spin-coating the P3HT onto the substrate and stamping the TiO_2 columns directly into the layer.

Figure 2.24 Chemical structures of P3HT and PCBM

Organic polymers are wider gap semiconductors. Thus, they give an efficient absorption in the near UV section of the electromagnetic spectrum. The gap of the P3HT:PCBM blend is approximately 1.8 eV. So the largest absorption wavelength should be around 650 nm, as shown in Figure 2.25. One of the interesting features of organic polymer is that the band gap can be easily altered, without changing the chemical components. It has been discovered that a Head-Tail alignment of P3HT has narrower gap that a Head-Head alignment. [63] It has also been discovered that, in several materials, a different arrangement in lateral chains can also result in different band gap structures. Moreover, changing the ratio of P3HT:PCBM can also change the band gap.[64]

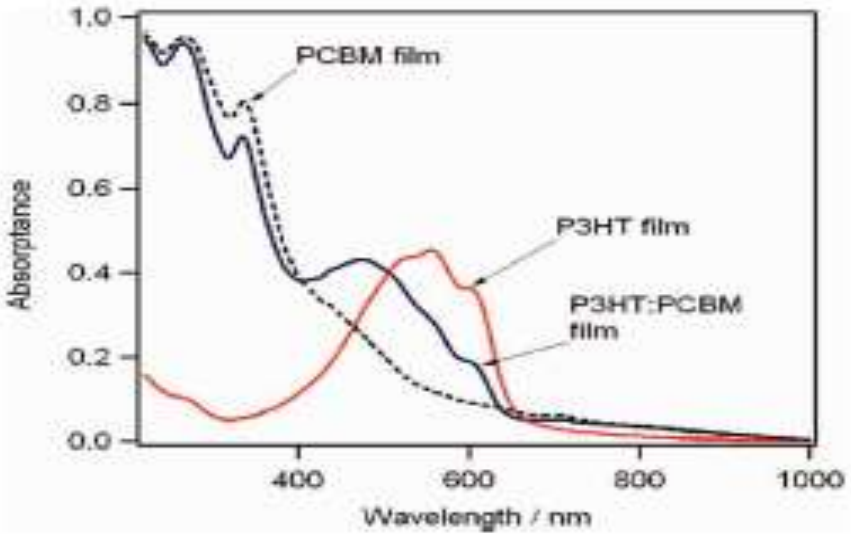

Figure 2.25Absorption spectral of P3HT film, PCBM film and P3HT:PCBM film

2.6.4 MEH-PPV

In OLEDs, the active layer is usually made of conjugated polymer. Among all the conjugated polymers, poly(1,4-phenylenevinylene) or PPV and its derivative 2-methoxy-5-(2-ethylhexyloxy)-p-phenylenevinylene or MEH-PPV have been studied extensively for OLED applications. Within the class of PPVs, a better choice for OLED application is MEH-PPV. This is due partly to its attractive solubility in solvents, which enables the processing of thin films. MEH-PPV is also used because of the reduction of crystallization of the polymer, when cast, and due to the fact that its valence and conduction bands are close to the work functions of the main materials used for electrodes. Such characteristics make MEH-PPV very favorable for charge injection and conduction in OLED devices. Moreover, it has been established that, the morphology of MEH-PPV films can be manipulated using different organic solvents, concentrations and spin speeds, thereby varying the optical and electrical properties of the resulting polymer films.[50]

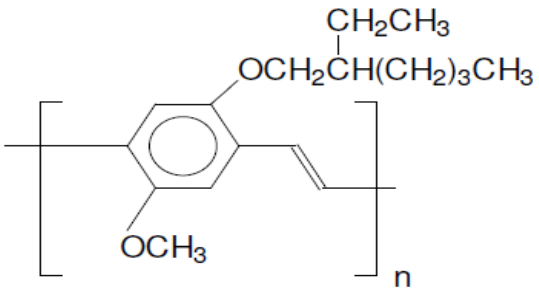

Figure 2.26 Chemical structure of MEH-PPV

2.6.5 Thin Film Deposition Techniques

The techniques that are used for thin-film deposition include; R.F Magnetron Sputtering, Spin Coating and Thermal Evaporation. These will be discussed in detail in this section.

Thermal evaporation is one of the simplest vacuum deposition methods and is widely used in industry. This is used to produce metallized paper and plastics for food packaging and labeling applications. Vacuum evaporation is a deposition method that involves the use of a source material that is evaporated in a vacuum environment. The vacuum allows vapor particles to travel directly to the target, object where they condense back to that solid state. An evaporation system includes a vacuum pump and an energy source which evaporates the material for deposition. The purity of the deposited film is a function of the vacuum quality and source material purity, while the film thickness varies with the geometry of the evaporation chamber, and the duration of evaporation.

Using the Evaporator

The evaporation process has 8 main steps:

1. Checking the System State
2. Venting the Chamber
3. Loading Metal and Samples
4. Evacuating the Chamber
5. Evaporating
6. Venting the Chamber
7. Unloading Metal and Samples
8. Evacuating the Chamber

Metal deposition by thermal evaporation is a high rate and wide web process. It can be used in a roll-to-roll coating line speeds exceeding 1000 m/min. However, depositing TCO films by thermal evaporation of the constituent metal has challenges not faced when depositing metal films. For example, if an indium-tin metal alloy is evaporated, oxygen must be provided and react with the indium and tin atoms to form the indium and tin oxides. The amount of added oxygen in the vacuum chamber must be kept low, typically creating a pressure of ~10^{-4} Torr (0.013Pa), which also may limit the surface reaction rate forming the TCO. Typically, this requires a substrate temperature of ~200^{o}C or more.[65]

Furthermore, the speed of this surface reaction is proportional to the substrate temperature and much higher temperatures are needed to achieve substantial reaction rates. Alternatively, instead of starting with the metals, the metal oxides, for example, indium and tin oxides can be vacuum evaporated, preferably from evaporation sources for better control to achieve the desired In-Sn composition in the oxide films.[65]

However, some oxygen is generally lost from the oxides during the evaporation process. Here, some oxygen background gas must be provided to achieve the desired oxide composition.

a)

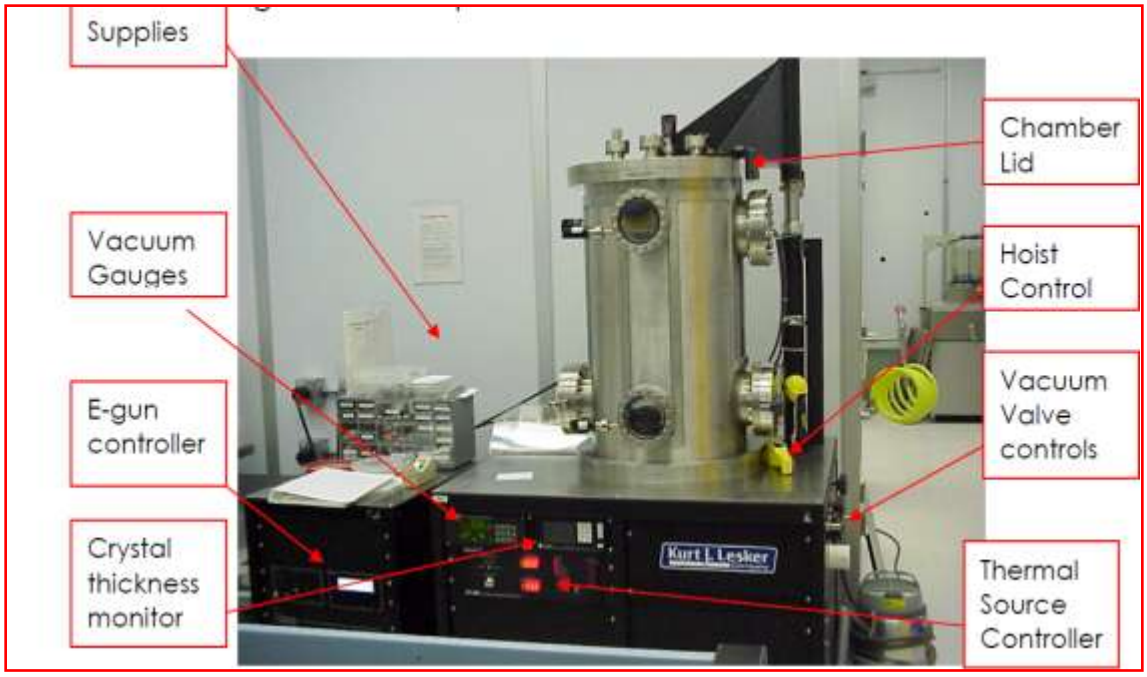

b)

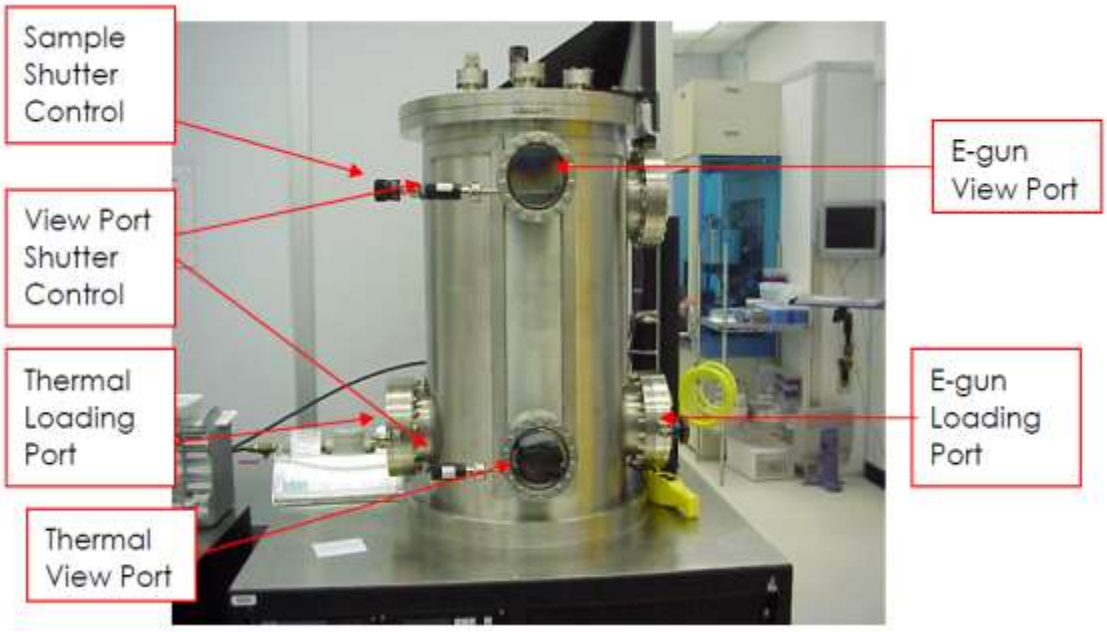

Figure 2.27 (a) System overview of the thermal evaporator (b) Outer chamber overview

2.6.6 Sputtering

Sputtering is the ejection of material from a target when bombarded by gas ions from plasma. These ions are attracted to the target by an applied electric field. The most common type of sputtering uses a DC electric field. Magnets placed behind the sputtering target (magnetrons) trap electrons increasing the ion bombardment of the target, hence increasing the deposition rate and also reducing substrate heating.[67] Sputtering is fundamentally a more energetic deposition process than evaporation.

However, it is not the arrival energy of the sputtered material on the substrate but the accelerated ions and neutrals from the plasma that bombard the growing film. This promotes adatom surface mobility and film densification resulting in a superior microstructures compared to those of evaporated films. [66] There are many implementations of the magnetron sputtering process. These include; direct current (DC), alternating current (AC), mid frequency (MF), radio frequency (RF), and in planar, cylindrical, inverse-cylindrical, rotatable and dual magnetron formats. However, DC magnetron sputtering is the dominant commercial ITO deposition method. The advantage of the RF Magnetron Sputtering is its less restrictive use for cases requiring high deposition rates and low substrate temperatures in both conducting and non-conducting targets.[67]

Figure 2.28 R.F Magnetron sputtering set-up

Four major benefits of magnetron sputtering sources are that (i) they scale easily in length permitting production coatings on very large substrates, (ii) they are compatible with temperature-sensitive substrates, e.g. plastic, (iii) they are able to operate at lower pressures (than diode sputtering) and (iv) the atomic compositions (metallic) of the deposited films are comparable to those of the target.[67]

2.6.7 Spin Coating Process Theory

Spin coating has been used for several decades for the application of thin films.

The most common technique used in the deposition of active and conducting layers in OLEDs and OSCs is spin coating. The theory of spin coating is based the centripetal acceleration force applied to a fluid which is deposited on the glass surface. It involves spreading a solution on a substrate by rotation at very high speeds. Final film thickness and other properties will depend on the nature of the resin (viscosity, drying rate, percent solids, surface tension, etc.) and the parameters chosen for the spin process. Factors such as final rotational speed, acceleration, and fume exhaust contribute to the properties of the coated films. Spin speeds determine the final thickness of material deposited. However, the velocity of the enveloped air (over the spinning substrate) also affects film thickness to an extent. For very thin films, the angular speed should be very high, as most solvents are volatile and evaporate concurrently.

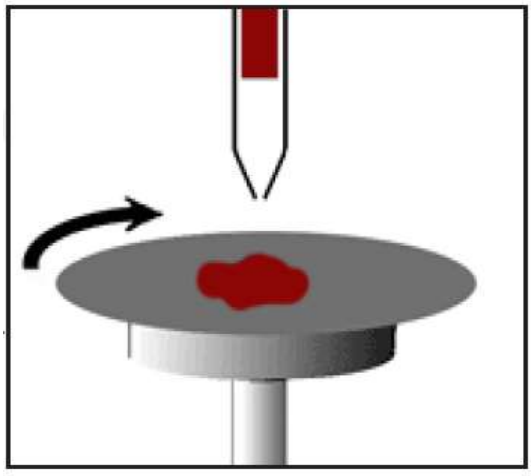

Figure 2.29 Illustration of spin coating

2.6.7.1Spin Coating Process Description

A typical process consists of a dispensing step, in which the resin fluid is deposited onto the substrate surface. A high speed spinning step is then used to thin the fluid, while a drying step is used to eliminate excess solvents from the resulting film. Two common methods of dispensing are Static dispensing, and Dynamic dispensing.

Static dispensing is simply the deposition of a small puddle of fluid on or near the center of the substrate. Dynamic dispense is the process of dispensing while the substrate is turning at low speed. A speed of about 500 rpm is commonly used during this step of the process. This serves to spread the fluid over the substrate and can result in less waste of resin material since it is usually not necessary to deposit as much to wet the entire surface of the substrate. The steps in the Spin Coating process are shown schematically in Figure 2.30.

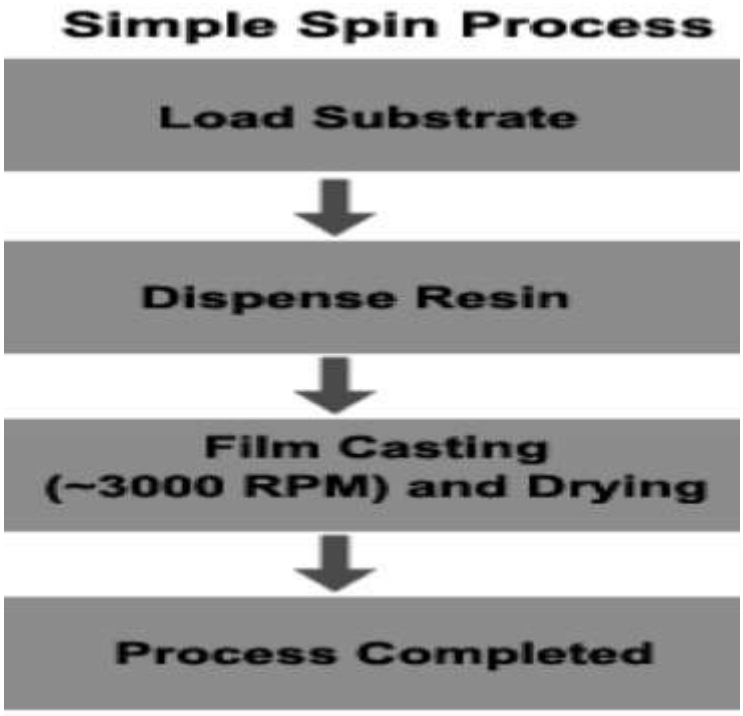

Figure 2.30 Simple spin coating process

The operation modes and spin parameters are all incorporated into a program recipe, which accompanies a spin coating process. The program recipe number containing how spin coating will be done are all displayed on the interface screen of the spin coating machine.

2.7. Characterisation of Device

2.7.1 Optical Characterisation

UV-visible micro-spectrophotometers consist of a UV-visible microscope integrated with a UV-visible spectrophotometer. These are commonly used for measuring thin film thickness in semiconductor manufacturing, materials science research, etc. The optical properties and band gap energy of thin films are investigated by UV-vis spectrometer.[68] Increased development in electronic technology has raised the need for understanding the optical and electrical properties of ITO. As a result, some of the solid state physics of ITO has also emerged. Although no concise and accurate knowledge is available, the literature survey indicates that many of these properties can be tailored by careful control of the deposition parameters. In OSC and OPV experiments, UV-vis spectrometer is used to measure the optical, such as the reflectance (R), transmittance (T) of thin films and evaluate the absorbance (A) and the semiconductor band-gap.[68]

2.7.1.1 Theory of UV-Visible Spectroscopy

The components of a typical spectrometer are presented in figure 2.31. The functioning of this instrument is relatively straightforward. A beam of light from a visible and/or UV light source (colored red) is separated into its component wavelengths by a prism or diffraction grating. Each

monochromatic (single wavelength) beam in turn is split into two equal intensity beams by a half-mirrored device. One beam, the sample beam (colored magenta), passes through a small transparent container (cuvette) containing a solution of the compound being studied in a transparent solvent. The other beam, the reference (colored blue), passes through an identical cuvette containing only the solvent. The intensities of these light beams are then measured by electronic detectors and compared. The intensity of the reference beam, which should have suffered little or no light absorption, is defined as $\mathbf{I_0}$. The intensity of the sample beam is defined as **I**. Over a short period of time, the spectrometer automatically scans all the component wavelengths in the manner described. The ultraviolet (UV) region scanned is normally from 200 to 400 nm, while the visible portion is from 400 to 800 nm.[67]

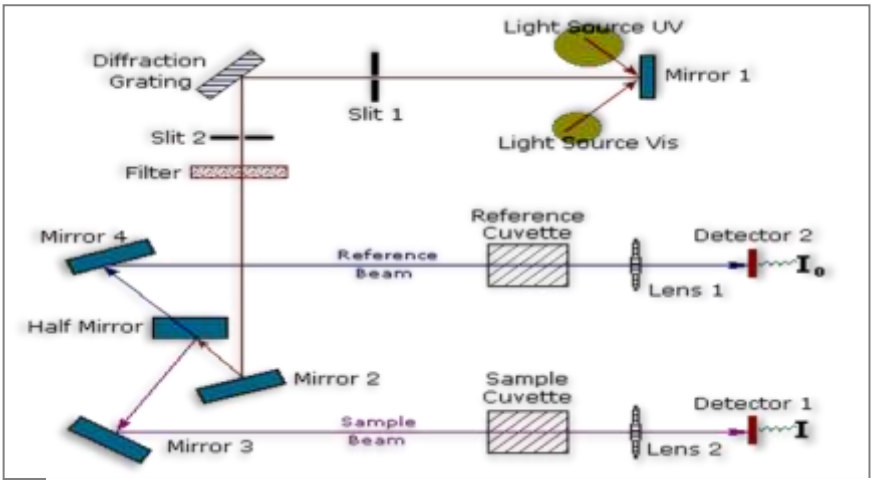

Figure 2.31 Schematic of a typical spectrometer

If the sample compound does not absorb light of a given wavelength, $\mathbf{I} = \mathbf{I_0}$. However, if the sample compound absorbs light then **I** is less than $\mathbf{I_0}$, and this difference may be plotted on a graph versus wavelength. Absorption may be presented as:

Transmittance: $T = I/I_0$ **(2.22)**

Absorbance: $A = \log I_0/I$ **(2.23)**

If no absorption has occurred, T = 1.0 and A= 0. Most spectrometers display absorbance on the vertical axis, and the commonly observed range is from 100% transmittance to 1% transmittance. The wavelength of maximum absorbance is a characteristic value, designated as λ_{max}.[68]

A common and simple method for determining whether a band gap is direct or indirect uses absorption spectroscopy. By plotting certain powers of the absorption coefficient against photon energy, one can normally tell both what value the band gap has, and whether or not it is direct.

For a direct band gap, the absorption coefficient α is related to light frequency according to the following formula:

$$\alpha \approx A^* \sqrt{h\nu - E_g} \qquad \textbf{(2.24)}$$

With $$A^* = \frac{q^2 \chi_{vc}^2 (2m_r)^{3/2}}{\lambda_0 \varepsilon_0 \hbar^3 n} \qquad \textbf{(2.25)}$$

where, α is the absorption coefficient, a function of light frequency ν, h is Planck's constant ($h\nu$ is the energy of a photon with frequency ν), $\hbar$ is reduced Planck's constant ($\hbar = h/2\pi$), E_g is the band gap energy, and A^* is a certain frequency-independent constant.

On the other hand, for an indirect band gap, the formula is:

$$\alpha \propto \frac{\left(h\nu - E_g + E_p\right)^2}{\exp\left(\frac{E_p}{kT}\right) - 1} + \frac{\left(h\nu - E_g - E_p\right)^2}{1 - \exp\left(-\frac{E_p}{kT}\right)} \qquad \textbf{(2.26)}$$

where, E_p is the energy of the phonon that assists in the transition, k is Boltzmann's constant and T is the thermodynamic temperature.

Therefore, if a plot of $h\nu$ versus α^2 forms a straight line, it can normally be inferred that there is a direct band gap, measurable by extrapolating the straight line to $\alpha = 0$ axis. On the other hand, if a plot of $h\nu$ versus $\alpha^{1/2}$ forms a straight line, it can normally be inferred that there is an indirect band gap, measurable by extrapolating the straight line to the $\alpha = 0$ axis (assuming $E_p \approx 0$).[87]

2.7.2 Morphological Characterization

The deposition technique with suitable deposition parameters adopted during thin-film analysis greatly determines the properties of the final surface. The most important property to be studied after the fabrication of HOILEDs and HOILSOLs is the layers roughness and thickness. A means of determining this is by using the surface profiler which makes use of extremely sensitive diamond tip to probe the surface of the layer. The surface profiler has a very fine tip, which scans the surface of the sample and this can be used to determine the film thickness, surface roughness and substrate waviness and sometimes stress measurement. The high aspect ratio tips are ideal for measuring shallow depths, trenches, or non-uniformities on the layer surface to the level.

2.7.3 Scanning Electron Microscope

The scanning electron microscope (SEM) is used to examine microscopic detail of solid specimens. SEM is also used to study the surface morphology of the layers relevant to the HOILEDs and HOISOLs. For instance, fractal dendritic structures can form with time. These reduce the distribution of PCBM structure in an OSC. They also affect the degree of charge hopping in the bulk heterojunction layer, and eventually the effective charge transport. The SEM can also be used to detect the presence of dust or any foreign particle at the interface of the layers relevant to the device. Figure 2.32 shows a clear SEM image of dust particle at the interface of a layered structure during cold welding of Au on Ag

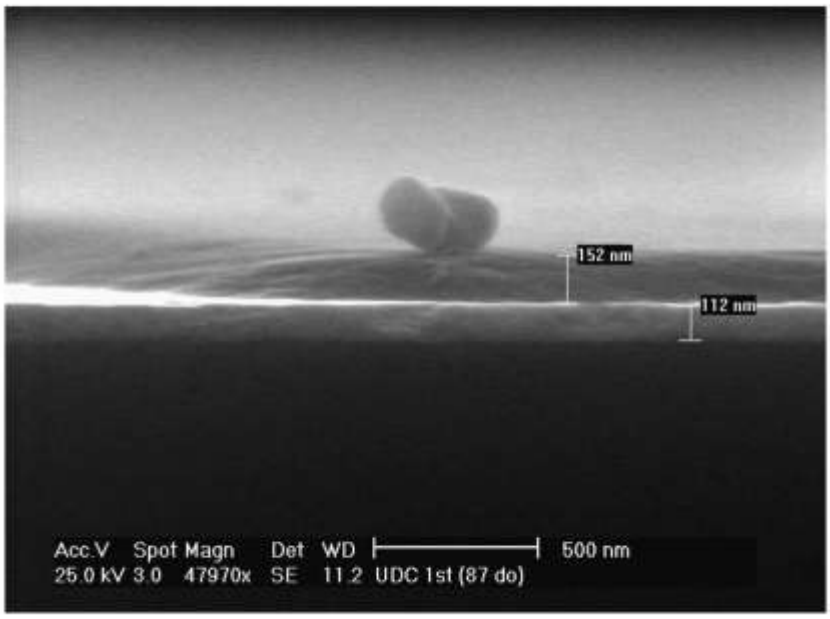

Figure 2.32 SEM image of dust particle in a semiconductor clean room

The SEM image is produced by scanning an extremely small focused beam of electrons (~0.5 -5 nm in diameter) across the surface of a specimen in an array of picture points (pixels) usually

1024 by 768 pixels. High–energy electron bombardment of the specimen causes different signals to be emitted at each pixel. These are collected and their intensities are used to produce images of the specimen by modulating the brightness of equivalent pixels on a monitor.

Initial viewing of the specimen uses the secondary electron emission signal to provide an image very similar in shape to the seen in the light microscope. These secondary electrons are ejected from the k-orbitals of the specimen atoms by inelastic scattering interaction with beam electrons and the sample. Due to their low energy, these electrons originate within a few nanometres form the sample surface. Unlike the light optical microscope that displays images in true colour, the SEM presents intensity images where zero signals is displayed as black, intermediate signals as shades of grey and maximum signal as white. Compared to the light microscope, SEM has three distinct advantages- better resolution, greater depth of field and the ability to carry out X-ray microanalysis.

Reference for Chapter 1 and 2

1. http://www.sciencedaily.com/news/earth_climate/energy/.

2. Mark Hankins "Solar Systems for Africa", June 2005, page 1-2.

3. C.W. Tang, S.A. VanSlyke, Appl.Phys.Lett. 51 (1987) 913.

4. J.H. Burroughes, D.D.C. Bradley, A.R. Brown, R.N. Marks, K. Mackay, R.H. Friend, P.L.Burns, A.B. Holmes, Nature, 247(1990)539.

5. http://en.wikipedia.org/wiki/Solar cells.

6. http://en.wikipedia.org/wiki/organic solar cells.

7. Serap Günes and Niyazi Serdar Sariciftci, "Hybrid Solar Cells", Inorganica Chimica Acta 361 (2008) 581–588.

8. Saunders, B.R.; Turner, M.L. (2008) *"Nanoparticle-polymer photovoltaic cells*", Advances in Colloid and Interface Science 138 (1): 1–23.

9. www.lios.at/publications/2004/2004-017.pdf.

10. J. L. Kyong Kon Kim, M. Namboothiry, David L. Carroll, *Applied Physics Letters* 90 (2007).

11. M. D. McGehee. "*Nanostructured Organic–Inorganic Hybrid Solar Cells"*. Materials Research Society Bulletin 34, 95 (2009).

12. Chin-Cheng Weng, Chia-Hung Chou, Kung-Hwa Wei1, and Jung Y. Huang, "*Enhanced Electroluminescence of Poly(2-methoxy-5-(20 -ethylhexyloxy)-1,4-phenylene vinylene) Films in the Presence of TiO2 Nanocrystals"***,** Journal of Polymer Research vol **13,** (2006) 229–235.

13. T. Tong, B. Babatope, S. Admassie, J. Meng, O. Akwogu, W. Akande, and W. O. Soboyejo, *"Adhesion in organic electronic structures".* Journal Of Applied Physics 106, 083708 (2009).

14. Su Zhan, Xie Ying-ge, Li Xia, Yu Tao*, Microelectronics Journal* 37 (2006) 714–71.

15. J. J. M. Halls, C. A. Walsh, N. C. Greenham, E. A. Marseglia, R. H. Friend, S. C. Moratti, and A. B. Holmes, *Nature 376,* 498 (1995).

16. G. Yu, J. Gao, J. C. Hummelen, F.Wudl, and A. J. Heeger, *Science 270*, 1789 (1995).

17. N. C. Greenham, X. Peng, and A. P. Alivisatos*, Phys. Rev. B 54*, 17628 (1996).

18. E. Becquerel, *Comptes Rendus*, 9, 561(1839).

19. R. Ohl, U.S. Patent 2,402,662 (1946).

20. *J. Appl. Phys*., 25, 676 (1954)

21. *"Light sensitive device"* U.S. Patent 2,402,662 Issue date: June 1946

22. Tomas Markvart '*Solar Electricity"* 2nd Ed.,Wiley, Chichester (2000),UK, pp 1-2;23-24, 28-31.

23. Solar Cell Efficiency Tables (Version12), Progress in Photovoltaics: Research and Applications 7 (1998. www.pv.unsw.edu.au/eff).

24. H. J. Lewerenz and H. Jungblut "Photovoltaic -Grundlagen und Anwendungen" *Springer*, Berlin, Hei-delberg, New York (1995).

25. Solar Energy Industry Research and Consultancy. Solarbuzz. Retrieved on 2011-01-19.

26. Tom Markvart and Luis Castañer, "Solar Cells: Materials, Manufacture and operation" 1st Edition,2005, pp 6,9-11,21.

27. http://www.doitpoms.ac.uk/tlplib/semicomductor.direct.php.

28. http://www.wikipedia.org/wiki/Direct_and_indirect _band_gaps.

29. Jenny Nelson "The Physics of Solar Cells", pp11-15.

30. Sam-Shajing Sun and Niyazi Serdar Sariciftci "*Organic Photovoltaics: Mechanics, Materials, and Devices"* 2005, pp.73-74, 113-116, 180-186, 434-439.

31. Memming,R., *"Photoelectrochemical solar energy conversion"* Topics Current Chem. 1988, Vol 143, pp.79-83.

32. http://en.wikipedia.org/wiki/File:Solar_Spectrum.png

33. Charles P. Poole Jr. and Frank J. Owens *"Introduction to Nanotechnology*", pp. 31-32

34. N. S. Sariciftci, *'Plastic photovoltaic devices', Materials Today 7(9), 36–40 (2004).*

35. H. Hoppe and N. S. Sariciftci*, Organic solar cells: an overview, J. Mater. Res. 19, 1924–1945 (2004).*

36. D. Sarti and R. Einhaus, *Solar Energy*. Mater. Solar Cells, 72, 27 (2002).

37. J. Cornil, D. Beljonne, J. P. Calbert, and J. L. Bredas, *Interchain interactions in organic pi-conjugated materials: impact on electronic structure, optical response, and charge transport,* Adv. Mater. 13, 1053–1067 (2001).

38. C. J. Brabec, N. S. Sariciftci, and J. C. Hummelen, *Plastic solar cells*, Adv. Funct. Mater. 11, 15–26 (2001).

39. I. G. Hill, A. Kahn, Z. G. Soos, and R. A. Pascal, *Charge-separation energy in films of pi-conjugated organic molecules*, Chem. Phys. Lett. 327, 181–188 (2000).

40. G. Yu, J. Gao, J. C. Hummelen, F. Wudl, and A. J. Heeger, *Polymer photovoltaic cells enhanced efficiencies via a network of internal donor–acceptor heterojunctions*, Science 270, 1789–1791 (1995).

41. N. S. Sariciftci, L. Smilowitz, A. J. Heeger, and F. Wudl,'*Photoinduced electron-transfer from a conducting polymer to buckminsterfullerene'*, Science 258, 1474–1476 (1992).

42. J. J. M. Halls, K. Pichler, R. H. Friend, S. C. Moratti, and A. B. Holmes, *Exciton diffusion and dissociation in a poly(p phenylenevinylene)/C-60 heterojunction photovoltaic cell,* Appl. Phys. Lett. 68, 3120–3122 (1996).

43. N. Corcoran, A. C. Arias, J. S. Kim, J. D. MacKenzie, and R. H. Friend*, Increased efficiency in vertically segregated thin-films conjugated polymer blends for light-emitting diodes*, Appl. Phys. Lett. 82, 299–301 (2003).

44. F. Padinger, R. S. Rittberger, and N. S. Sariciftci*, Effects of postproduction treatment on plastic solar cells,* Adv. Funct. Mater. 13, 85–88 (2003).

45. Murray, C. B.; Norris, D. J., and Bawendi, M. G. *Synthesis and characterization of nearly monodisperse CdE (E=S, Se, Te) semiconductor nanocrystallites*. J. Amer.Chem. Soc. 1993, 115(19): 8706–8715.

46. O'Regan, B. and Gratzel, M. A. *Low-cost, high-efficiency solar-cell based on dye-sensitized colloidal TiO_2 films*. Nature 1991, 353(6346), 737–740.

47. Salafsky, J. S.; Lubberhuizen, W. H., and Schropp, R. E. I. *Photoinduced charge separation and recombination in a conjugated polymer-semiconductor nanocrystals composite.* Chem. Phys. Lett. 1998, 290(4–6), 297–303.

48. Salafsky, J. S. *Exciton dissociation, charge transport, and recombination in ultrathin, conjugated polymer– TiO_2 nanocrystal intermixed composites*. Phys. Rev. B 1999, 59(16), 10885–10894.

49. van Hal, P. A.; Wienk, M. M.; Kroon, J. M.; Verhees, W. J. H.; Slooff, L. H.; van Gennip, W. J. H.; Jonkheijum, P., and Janssen, R. A. J. *Photoinduced electron transfer and photovoltaic response of a MDMO-PPV:TiO2 bulk-heterojunction*. Adv. Mater. 2003, 15(2), 118–121.

50. B. A. Gregg, M. A. Fox, and A. J. Bard, *J. Phys. Chem*. 94, 1586 (1990).

51. B. A. Gregg and Y. I. Kim, *J. Phys. Chem*. 98, 2412 (1994).

52. G. G. Malliaras, J. R. Salem, P. J. Brock, and J. C. Scott, *J. Phys*. 84, 1583 (1998).

53. C. J. Brabeck, A. Cravino, D. Meissner, N. S. Sariciftci, T. Fromherz, M. T. Rispens, L. Sanchez, and J. C. Hummelen, *Adv. Funct. Mater*. 11, 374 (2001).

54. C. M. Ramsdale, J. A. Barker, A. C. Arias, J. D. MacKenzie, R. H. Friends, and N. C Greenham, *J. Appl. Phys.* 92, 4266 (2002).

55. W. R. Salaneck, S. Stafstrom, and J. L. Bredas, *Conjugated Polymer Surfaces and Interfaces* (Cambridge University Press, Cambridge, 1996).

56. H. Ishii, K. Kiyoshi, E. Ito, and K. Seki, *Adv. Mater*. 11, 605 (1999).

57. Y. Gao, *Surface analytical studies of interface formation in organic light emitting devices,*Acc. Chem. Res. 32, 247 (1999).

58. E. W. Forsythe and Y. Gao, *Handbook of Surfaces and Interfaces of Materials*, H. S. Nalwa, ed., p. 286 (Academic Press, New York, 2001).

59. G.P. Evens, *Adivance in Electrochemicals science and Engineering*, Vol.1,VCH Verlagsegesell Schaft mbH, (1990).

60. Jinsong Huang, Gang Li, and Yang Yang, *A Semi-transparent Plastic Solar Cell Fabricated by a Lamination Process Adv. Mater.* 2008, *20*, 415–419.

61. C. Giebeler, H. Antoniadis, D. D. C. Bradley, and Y. Shirota, *J. Appl. Phys*. 85, 608 (1999).

62. Q. T. Le, F. Nuesch, L. J. Rothberg, E. W. Forsythe, and Y. Gao, *Appl. Phys. Lett*. 75, 1357 (1999).

63. Al-lbrahim, M.; Ambacher, O. "*Effects of solvent and annealing on the improved performance of solar cells based on poly(3-hexylthiophene): Fullerene*". Appl.Phys.Lett. 86 201120 (2005).

64. Cook, S.; Katoh, R.; Furube, A. "*Ultrafast Studies of Charge Generation in PCBM:P3HT.*

65. *Blend Films following Excitation of the Fullerene PCBM*" J.Phys.Chem.C. 113(6), (2009) pp-2547-2552.

66. Antonio Facchetti and Tobin J. Marks. *Transparent Electronics: From Synthesis to Application*. John Wiley and Sons, Ltd (2010(pp 116-118).

67. W. D. Westwood, *Sputter Deposition*, in AVS Education Committee Book Series, Vol. 2, H. G. Thompkins (Ed.), AVS, New York, 2003.

68. S. Cheylan, J. Puigdollers, C. Voz, R. Alcubilla and G. Badenes; *Optical and Electrical characteristics of LEDs based on a single organic layer.*

CHAPTER THREE

3.0 Introduction

This work is based on the prior work done by Akande et al. [2,9], on the study of adhesion in cold-welded Au-Ag interface that are relevant to the fabrication of organic electronic structures.

In their work, focused ion beam, transmission electron microscopy and electron energy loss spectroscopy techniques were used to reveal interfacial impurities associated with the cold welding of nanoscale Au and Ag thin films. A theoretical model was also developed and used to predict the contact profiles around impurities between cold-welded thin films. The model was shown to provide new insights into how adhesion affects the surface contacts that occur during cold welding.[2,8,9] Also work done by Cao et al.[11], presented the effects of dust particles and layer properties on organic electronic devices fabricated by stamping.

Therefore, this work seeks to come out with an analytical approach on modeling the surface contacts of these electronic devices.

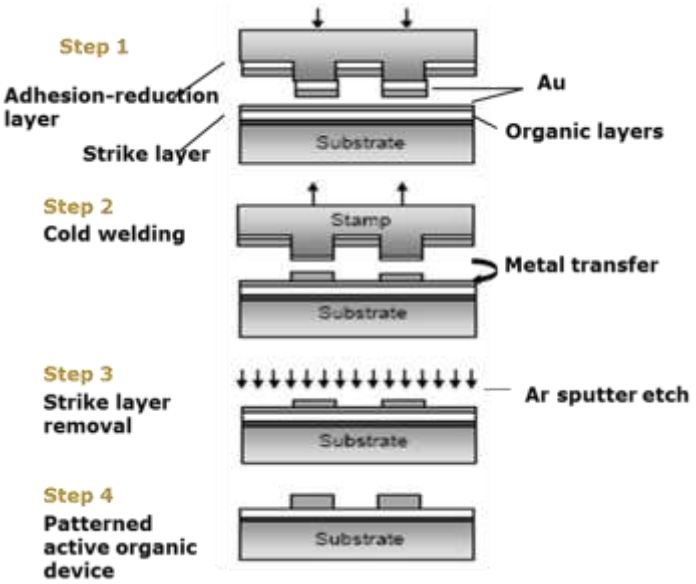

Figure 3.1 (a) Schematic of steps in cold welding of two metals [2]

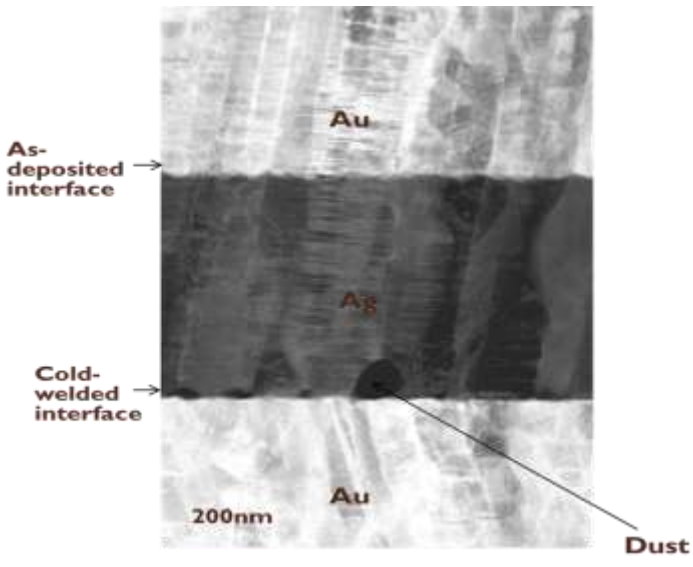

Figure 3.1 (b) TEM images of cold welded Au-Ag film [11]

Cold welding or cold pressure welding is the process by which clean, Oxide-free metallic surfaces are brought together to achieve intimate contact and hereby form metallic bonds. The technique is now employed in the fabrication of OLED, aforementioned. This process is illustrated in the schematic in Figure 3.1. In step 1 and step 2, a stamp with a metal layer is pressed onto a substrate with a pre-deposited, thin metal "strike" layer. Cold welding occurs as a result of intimate contact between the two clean metal surfaces. In step 3 and step 4, pressure is being applied on the stamp to ensure more contact, the finally, in step 4, metal transfer from stamp to substrate occurs by separating the stamp and substrate, where the strong cold welds parts the film from the stamp due to its relatively weak adhesion to the stamp surface.

Lamination process is also a technique employed in the fabrication of electronic devices.[60] This printing method involved transferring the spin coated Al-cathode onto the spin coated P3HT:TiO_2 films at room temperature by applying moderate pressure (between 10–70 MPa) to avoid 'sink-in'. Prior work by *Hong et al.*[19] using lamination techniques has shown the presence of dust particles as defects between the laminated interfaces. Presence of dust/TiO_2 particles decreases the lifetime and performance of laminated organic devices.

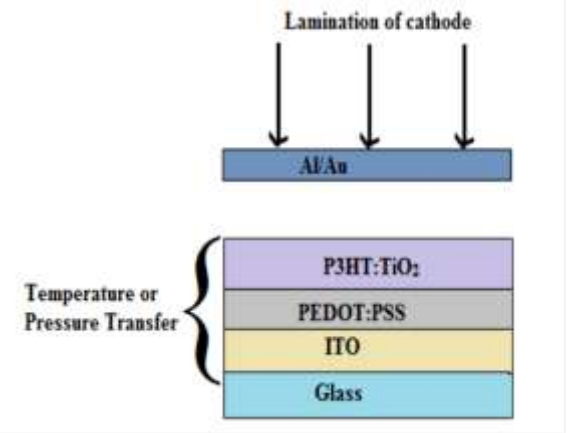

Figure 3.11 (a) Schematic of laminated HOISOL

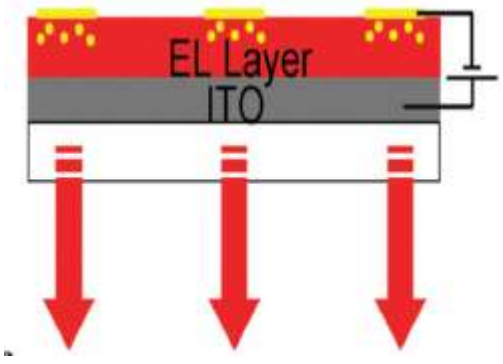

Figure 3.11 (b) Illustration of Sink-in of particles into layers

3.1 Adhesion Energy Measurement

Adhesion can be described as any attraction process between dissimilar surfaces that forms direct contact with each other due to bonding at the atomic scale. The most common force of attraction that exists between adhesive contacts is Van der Waals force of attraction. However contacts may also result from hydrogen bond or primary bonds between the surfaces.

Adhesion Energy is determined through the Derjaguin–Muller–Toporov (DMT) model that characterizes weak interactions between stiff materials with small radii.[13] The DMT model requires the determination of adhesion forces and the effective radius between the layers of the HOISOLs and the HOILEDs**.**

In order to determine these properties, Atomic Force Microscopic, AFM, technique is employed. This is a recent technique used to investigate the surface morphology of OPVs. It is an imaging technique that typically maps a surface with respect to surface topography as shown, schematically in the Figure 3.12.

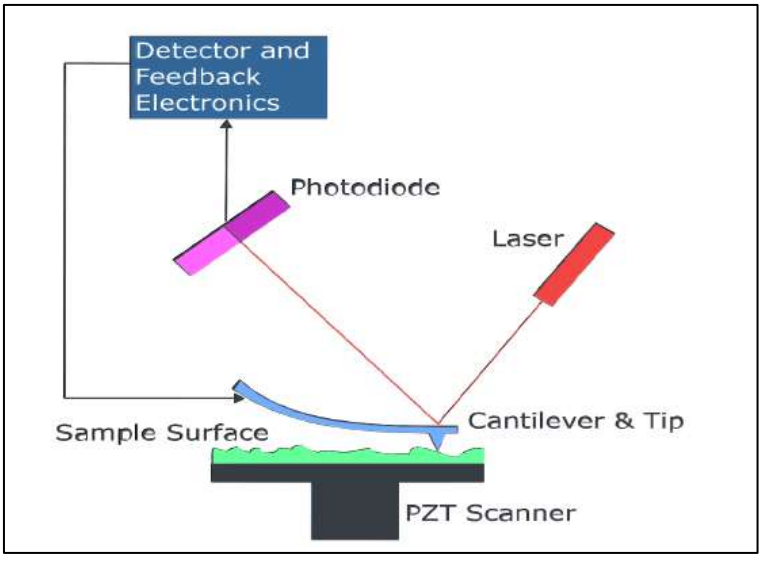

Figure 3.12 Schematic of Atomic Force Microscope (AFM)

First, the micro fabricated cantilever probe is attached to a scanner head that is lowered towards the surface at a constant velocity. The tip deflection is close to zero and experiences negligible interaction with the surrounding medium at ambient conditions. However, as the tip is lowered down, the tip is pulled into contact with the surface by adhesive force interaction between the tip of the probe and the surface.[8]

Afterwards, the scanner continues in the downward motion with the substrate and probe in continues contact, causes the tip to bend under elastic deformation. When the tip displacement direction is reversed, the scanner head lifts up and the tips elastic deformation is reversed, whereas the residual adhesive interaction prevents the tip from separating from the substrates surface at zero loads. [8] Therefore, the reversed loading of the tip must be continued until the adhesive forces are eventually overcome at a negative force that corresponds to the pull-off force. These steps and displacement curves for the AFM technique are illustrated in Figure 3.12. The measured displacement deflection can then be related to the adhesion force via Hooke's Law given as:

$$F = kx \tag{3.1}$$

Where k is the spring constant and x is the tip displacement. The accuracy of the AFM measurements of the adhesion force depends substantially on the measurement of the spring constant, k, of the AFM cantilever tip.

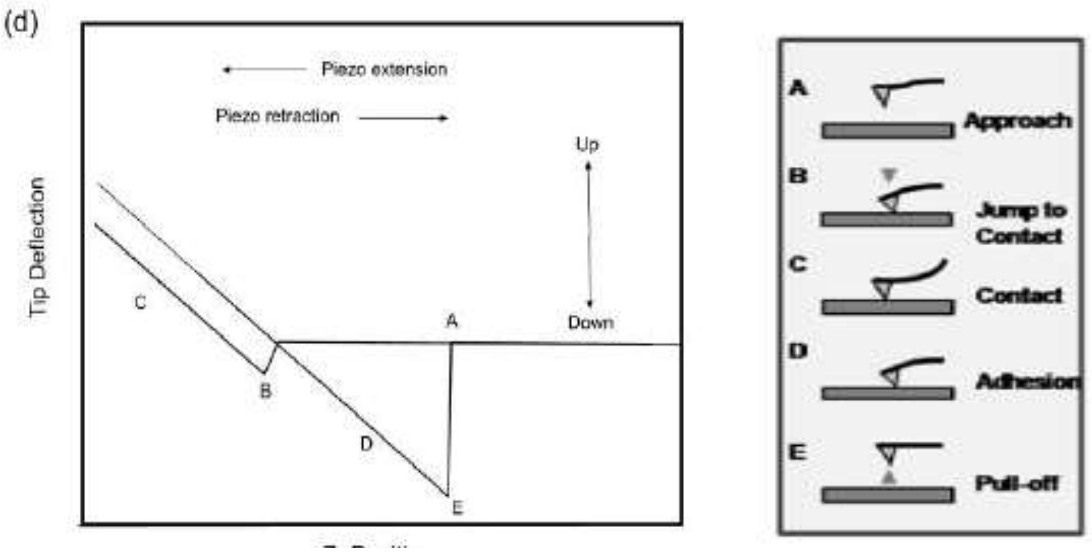

Figure 3.12 Model displacement curve for the AFM pull-off technique, (b) Corresponding physical description of points A-E on the displacement curve [2]

3.1.1 Adhesion Energy Modeling and Interfacial Fracture Mechanics

The adhesion force between two surfaces can be measured to find the adhesion energy γ required to separate these layers. This correspond to the knowledge related to the mode I energy, G from a fracture mechanics standpoint. For crack growth between two dissimilar materials (1 and 2), with surfaces of energies γ1 and γ2, the adhesion energy will be:

$$G_{adhesion} \sim G_{elastic} = \gamma_{surface\ 1} + \gamma_{surface\ 2} - \gamma_{surface\ 12} \quad \textbf{(3.11)}$$

Variety of models that predict the contact area for various geometries have a long history, dating back to the pioneering work of Hertz in 1881[18] Hertz found that the radius of the circle of contact $a_{surface}$ was related to the indenter load P, the spherical indenter radius R, and the elastic properties of the contacting materials by:

$$a_{surface}^3 = \frac{PR}{K} \quad \textbf{(3.12)}$$

Where *R* is the equivalent radius and *K* is the equivalent elastic modulus of the indenter tip and the sample, given by :

$$\boldsymbol{K = \frac{4}{3}\left(\frac{1-v_1^2}{E_1} + \frac{1-v_2^2}{E_2}\right)^{-1}} \quad \textbf{(3.13)}$$

where E and v are the Young's modulus and the Poisson's ratio, respectively, and subscripts 1 and 2 denote the indenter and the sample, respectively.

Different adhesion models exist based on varying material and geometric properties of interacting layers. The Derjaguin-Muller-Toporov (DMT) model[13] applying to weak interactions between stiff materials with small radii; In this case, the adhesion energy is related to the adhesion force by:

$$\boldsymbol{\gamma_{DMT} = \frac{F_{adhesive}}{2\pi R}} \quad \textbf{(3.14)}$$

Also, the Johnson-Kendall-Robert (JKR) model[14] which considers strong interactions between compliant materials with large radii. The JKR model for electric contact incorporated adhesion into Hertzian contact model by formulating a theory of adhesive contact using a balance between the stored elastic energy and the loss in surface energy. The general solution for the pressure distribution in the contact area is given by:

$$P(r) = P_0\left(1 - \frac{r^2}{a^2}\right) + P_0'\left(1 - \frac{r^2}{a^2}\right)^{\frac{-1}{2}} \quad \textbf{(3.15)}$$

where the following parameters are defined as follows:

$$P_0 = \frac{2aE^*}{\pi R} \quad \textbf{(3.16)}$$

$$P_0' = -\left(\frac{4\gamma E^*}{\pi A}\right)^{\frac{1}{2}} \quad \textbf{(3.17)}$$

$$\frac{1}{R_i} = \frac{1}{R_1} + \frac{1}{R_2} \qquad (i = 1,2) \quad \textbf{(3.18)}$$

$$\frac{1}{E^*} = \frac{1-v_1^2}{E_1} + \frac{1-v_2^2}{E_2} \quad \textbf{(3.19)}$$

Where $\boldsymbol{a}$ is the radius of the area of contact, $\boldsymbol{2\gamma}$ is the total surface energy of both surfaces per unit contact area, $\boldsymbol{R_i}$, is the radii of the two contact surface, $\boldsymbol{E^*}$ is the Young's moduli and $\boldsymbol{v}$ is the Poisson's ratio.

The distance between the two spheres is given as:

$$d = \frac{\pi a}{2E^*}(P_0 + 2P_0') = \frac{a^2}{R} \quad \textbf{(3.20)}$$

The Hertz equation for the contact area between the two spheres modified to take into consideration the surface energy is:

$$a^3 = \frac{3R}{4E^*}\left(F + 6\gamma\pi R = \sqrt{12\gamma\pi RF + (6\gamma\pi R)^2}\right) \quad \textbf{(3.21)}$$

Simplifying the above equation (3.21) with a zero surface energy returns to the Hertzian condition given by:

$$a^3 = \frac{9R^2\gamma\pi}{E^*} \quad \textbf{(3.22)}$$

The pull-off force can be described as the tensile load at which the spheres are separated, that's the radius of contact are a = 0 and this force is independent of the moduli of the two spheres. This is given by:

$$F_C = -3\gamma\pi R \quad \textbf{(3.23)}$$

By combining all these relevant equations, the JKR model radius can then be written as:

$$a^3 = \frac{3R}{4E^*}\left(F + 3\Delta\gamma\pi R + \sqrt{6\Delta\gamma\pi RF + (3\Delta\gamma\pi R)^2}\right) \quad \textbf{(3.24)}$$

with the tensile load at separation given by:

$$F = -\frac{3}{2}\Delta\gamma\pi R \quad \textbf{(3.25)}$$

Hence the in JKR model, the adhesion force and energy are related by:

$$\boldsymbol{\gamma_{JKR} = \frac{2F_{adhesive}}{3\pi R}} \quad \textbf{(3.26)}$$

where γ_{JKR} is the JKR model adhesive energy, $F_{adhesive}$ is the adhesive force. The relation between the adhesive and energy for the JKR- model is presented in equation (3.26). Note that the negative sign denotes opposing sense between the two measured quantities. The JKR model applies to strong adhesive forces compliant materials with large radii.

The Maugis-Dugdale (MD) model[15] which lies between the DMT and JKR models. These models continue to form the basis for obtaining the adhesion energies from adhesion forces. An iterative method has been developed by Capick et al., Pietrement, and Tryon [16,17] which gives an approximation of the MD adhesion energy to within 1% accuracy. These calculations require knowledge of a combination of material and geometric properties and can be used to characterize the entire range of adhesion models through the calculation of a non-dimensional parameter, λ.

$$\lambda = 2\sigma_o(R/\pi K^2\gamma)^{1/3} = -0.913\ln(1 - 1.1018\alpha) \quad \textbf{(3.27)}$$

Where R is the effective radius given by equation 3.18 and K is a constant given by equation 3.13. σ_0 is the constant adhesive force between both bodies and it is non-zero at small distances. Hence the adhesion energy for MD model is given by:

$$\boldsymbol{\gamma = \frac{G}{2} = \frac{F_{ad}}{\pi R\overline{F_{ad}}}} \quad \textbf{(3.28)}$$

where $\overline{F_{ad}} = 0.267\alpha^2 - 0.767\alpha + 2$. Value of $\lambda < 0.1$, $\lambda > 5$ and $0.1 < \lambda < 5$ corresponds to the DMT, JKR and MD models respectively. The above equations for DMT, JKR and MD models are useful for conversion of pull-off forces, obtained from AFM adhesion experiments.

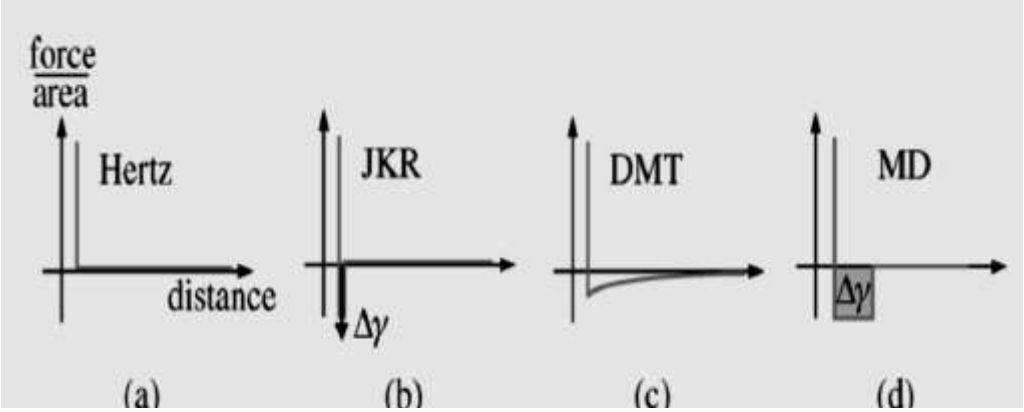

Figure 3.13 Typical force per unit area displacement curve for: (a) Hertz, (b) JKR, (c) DMT and (d) Maugis-Dugdale (MD) adhesion models regarding contact theory of spheres

From Figure 3.13, the JKR model includes only a short-range adhesion in the contact area; actually it is a δ function with the work of adhesion $\Delta\gamma$. The DMT model shows a long-range surface force which acts outside the radius of the circle of contact. The MD model considers the Dugdale (square well) potential to describe attractive forces.

3.1 Analytical Modelling of Contacts

In this model, the elastic wrapping around the TiO_2 particles is analogous to a cantilever deflection of a rigid particle. To explain the effect of the presence of the TiO_2 particle at the interface, the energy balance approach is employed in this analytical work. Also, it was assumed that, the TiO_2 particle is rigid, the deflection δ is approximately equal to the height of TiO_2 particle at the interface and there is no sink-in of the particle. Below are schematics of the contact between laminated top contact and the underlying surface in the presence of TiO_2 particles.

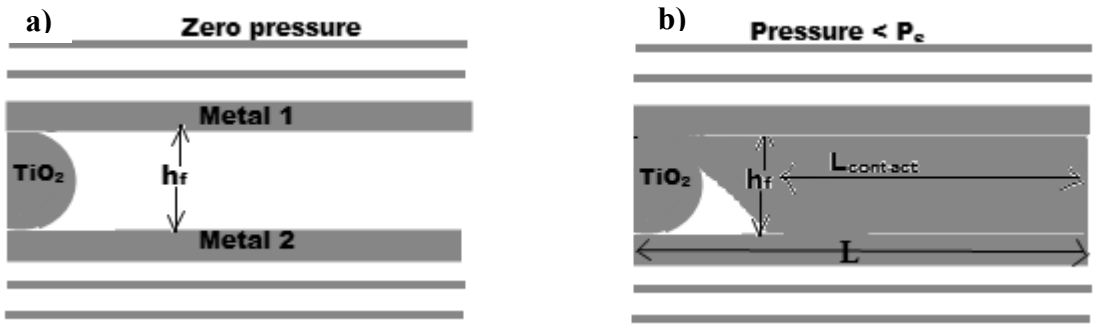

Figure 3.14 Contact between cold welded/laminated top contact and underlying surface in the presence of titania particles

In figure 3.14, (a) shows the initial approach of the two surfaces to be laminated with the TiO_2 particle embedded on the surface of metal 2 and (b) shows metal elastically deforms around the TiO_2 particle (S-shaped).

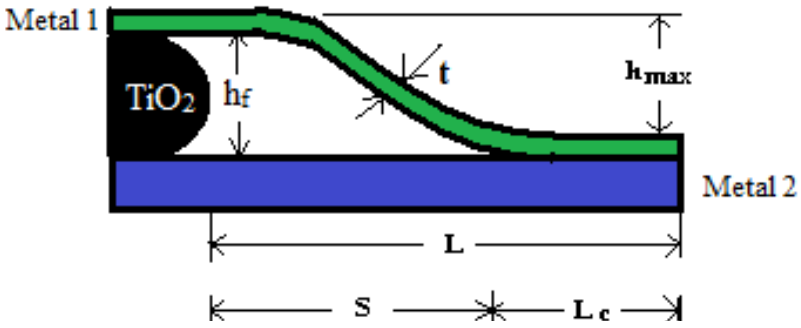

Figure 3.15 S-shaped contact between elastically deformed laminated surface

Consider the cantilever beam of length L, below (Figure 3.16), subject to bending (deflection of beam). This assumes that the particle is rigid, the system is linear-elastic, and therefore the deflection δ is a linear function of F. The total strain energy stored in the system is the sum of the individual strain energies.

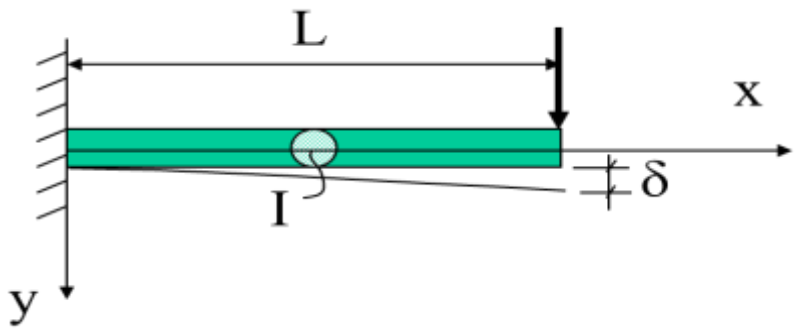

Figure 3.16 Cantilever beam subject to bending

The moment is given as:

$$M = F(x - L) \quad \textbf{(1)}$$

Thus the strain energy in the entire beam is given as:

$$U = \int_0^L \frac{[F(x-L)]^2}{2EI} dx \quad \textbf{(2)}$$

$$U = \frac{F^2 L^3}{6EL} \quad \textbf{(3)}$$

$$External\ work: W = \frac{1}{2} F\delta = Strain\ Energy$$

$$\frac{1}{2} F\delta = \frac{F^2 L^3}{6EI}$$

So the deflection of the beam is given as:

$$\boldsymbol{\delta = \frac{FL^3}{3EI}} \quad \textbf{(4)}$$

where M is the moment, U is the strain energy, E is the Young's modulus, F is the applied force, L is the beam length and I is the second moment of area.

The deflection, $\boldsymbol{\delta}$, as shown in Figure 3.16, is assumed to be approximately equal to the height of TiO_2 particle, $\boldsymbol{h_f}$, at the layered interface shown in Figure 3.15. Hence, $\boldsymbol{h_f}$, can be evaluated using equation (4) to give:

$$\boldsymbol{h_f = \frac{FL^3}{3EI}} \quad \textbf{(5)}$$

3.2.1 Derivation of Elastic (Strain) Energy of Entire System

From prior works done by Cao et al. [11] and Akande et al.[9], the presence of defect at the layered interface of organic electronic devices, can be of two different shapes. That is the S-shaped with long length and the arc-shaped with tip nearly attached to the surface, as shown in Figure 3.17.

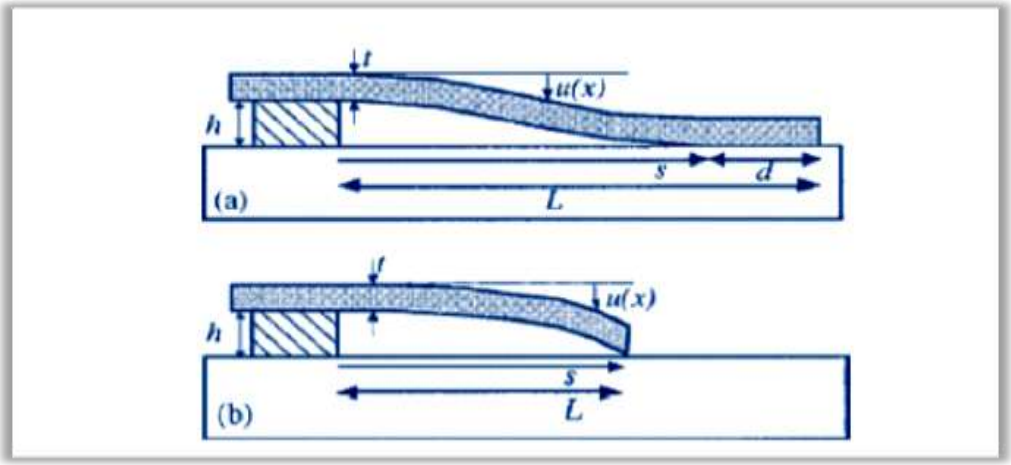

Figure 3.17 (a) S-shaped film attached over a long length (b) Arc-shaped film attached only very near its tip

For the first case, let's consider the elastic energy stored in the layer due to bending for the arc-shaped deflection. This is given as, the sum over the entire length given in equation (2).

Integrating this equation (2) within the limits of 0 to *s*, where s is the void length, the elastic energy for arc-shape is obtained to be:

$$\boldsymbol{U_{e\,Arc-shape} = \frac{F^2 s^3}{6EI}} \quad \textbf{(6)}$$

From equation (4), the applied force, F, is given by:

$$F = \frac{3EI}{s^3} h_f \quad \textbf{(7)}$$

Substituting equation (7) into equation (6), the elastic energy in terms of h_f, is obtained as :

$$U_{e\,Arc-shape} = \frac{(\frac{3EI}{s^3} h_f)^2 s^3}{6EI} = \frac{9E^2 I^2 s^3 h_f^2}{6EIs^6} \quad \textbf{(8)}$$

$$\boldsymbol{U_{e\,Arc-shape} = \frac{3}{2}\frac{EI}{s^3} h_f^2} \quad \textbf{(9)}$$

From prior work by Zong et al. [10], the total energy of the system as shown in the figure 3.17 (a), is the sum of the elastic energy stored in the beam due to the bending (S-shape). Similarly, from the same approach, the elastic energy for S-shape is given by:

$$\boldsymbol{U_{e\,s-shape} = \frac{6EI}{s^3} h_f^2} \quad \textbf{(10)}$$

where $U_{e\ s\text{-}shape}$ and $U_{e\ \ Arc\text{-}shape}$, are the strain energies for S-shape and arc-shape respectively, *E* is the Young's modulus, h_f is the height of TiO_2 particle, *s* is the void length and *I* is the second moment of area.

3.2.2 Modeling of Contact in Organic and Hybrid Organic/Inorganic Structures

From Figure 3.15 above, the contact length, L_c, is given by:

$$\boldsymbol{L_c = L - s} \quad \textbf{(11)}$$

where $\boldsymbol{s}$ is the length between the particle and the point of contact of between layer 1 and the layer 2. To know the real contact length, L, the void length, s, must be determined.

From fracture mechanic and the energy balance approach, the total energy of a system, U_T, under deformation is given by the sum of the elastic energy, U_e and the surface energy U_s of the system:

$$\boldsymbol{U_T = U_e + U_s} \quad \textbf{(12)}$$

In the previous section 3.2.1, the elastic energy for arc-shape and S-shape were derived.

3.2.2.1 Void Length for Arc-shape

From the energy balance approach, the total energy for the system in Figure 3.17 (b), is given as:

$$U_T = U_{e_{Arc-shape}} + U_s \quad \textbf{(13)}$$

Where the surface energy is given as:

$$U_s = \gamma b L_c \quad \textbf{(14)}$$

Therefore, $U_T = U_{e_{Arc-shape}} + \gamma b L_c$ **(15)**

Substituting equations (9) and (11) into equation (15), we have:

$$U_T(s) = \frac{3}{2}\frac{EI}{s^3}h_f^2 + \gamma b(L - s) \quad \textbf{(16)}$$

At equilibrium, the total energy $\boldsymbol{U_T(s)}$ of the system has a minimum corresponding to the void length $\boldsymbol{s}$. This is found by setting the derivative of the total energy with respect to s to zero.

Thus; $$\frac{dU_T(s)}{ds} = -\frac{9}{2}\frac{EIh_f^2}{s^4} + \gamma b = 0 \quad \textbf{(17)}$$

Upon simplifying, a relation between the void length, Young's modulus, surface energy and height of defect, is obtained to be:

$$\boldsymbol{S^4_{Arc-shape} = \frac{9EIh_f^2}{2\gamma b}} \quad \textbf{(18)}$$

But, the second moment of area is given as:

$$I = \frac{bt^3}{12} \quad \textbf{(19)}$$

Substituting I into equation (18) yields:

$$S^4_{Arc-shape} = \frac{9}{24}\frac{Ebt^3h_f^2}{\gamma b}$$

$$\boldsymbol{S^4_{Arc-shape} = \frac{3}{8}\frac{Et^3h_f^2}{\gamma}} \quad \textbf{(20)}$$

Therefore, the relation between the void length, $\boldsymbol{s}$, Young's modulus, $\boldsymbol{E}$, surface energy $\boldsymbol{\gamma}$ and height of defect, $\boldsymbol{h_f}$ is obtained to be:

$$\boldsymbol{S_{Arc-shape} = \left(\frac{3}{8}\frac{Et^3}{\gamma}h_f^2\right)^{1/4}} \quad \textbf{(21)}$$

3.2.2.2 Void Length for S-shape

Similarly, using the energy balance approach and the elastic energy obtained for S-shape in equation (10), the relation for void length is obtained. In this case, the total energy of the system (in Figure 3.15), is:

$$\boldsymbol{U_T = U_{e_{S-shape}} + U_s} \quad \textbf{(22)}$$

Thus the void length for S-shape is given as:

$$S_{S-shape} = \left(\frac{3}{2}\frac{Et^3}{\gamma}h_f^2\right)^{1/4} \quad (23)$$

where S is the void length, Young's modulus, E, surface energy γ , t is the thickness of film and h_f is the height of TiO_2 particle. Thus, by knowing the adhesion energy, γ, between the two interacting materials (Figure 3.15), the void lengths associated with a particular condition of pressure-assisted lamination and cold welding, can be calculated.

CHAPTER FOUR

4.0 Results and Discussions

The equations obtained for void length for arc-shape and s-shape films, can be used to investigate the effects of pressure, adhesion and height of TiO_2 nanoparticle on the contact length during fabrication of hybrid electronic devices by cold welding or lamination. To predict contact lengths, the adhesion energy, γ, has to be measured using the AFM pull-off technique as discussed in sections 3.1 and 3.2. For this model calculations, AFM results obtained from prior work done by Akande et al.[2] and Tong et al.[8], were used in the calculation. Below in Figure 4.1, shows the adhesion energies for different layers in OLEDs and HOILEDS; and Figure 4.11 show the results for adhesion energies for different layers in OSOLs.

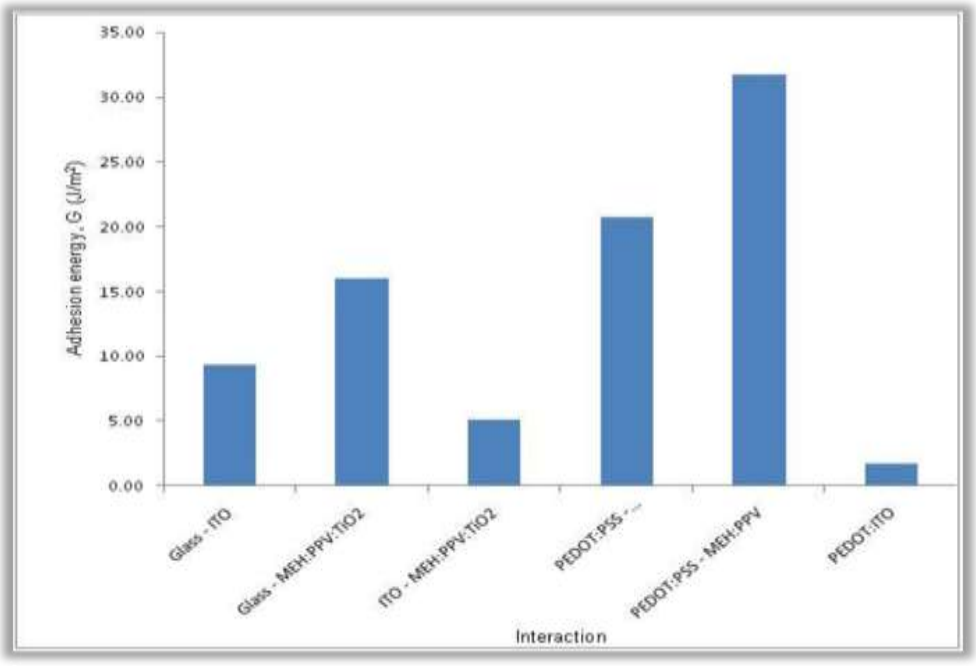

Figure 4.1 Adhesion energy for different layers in OLEDs/HOILEDs

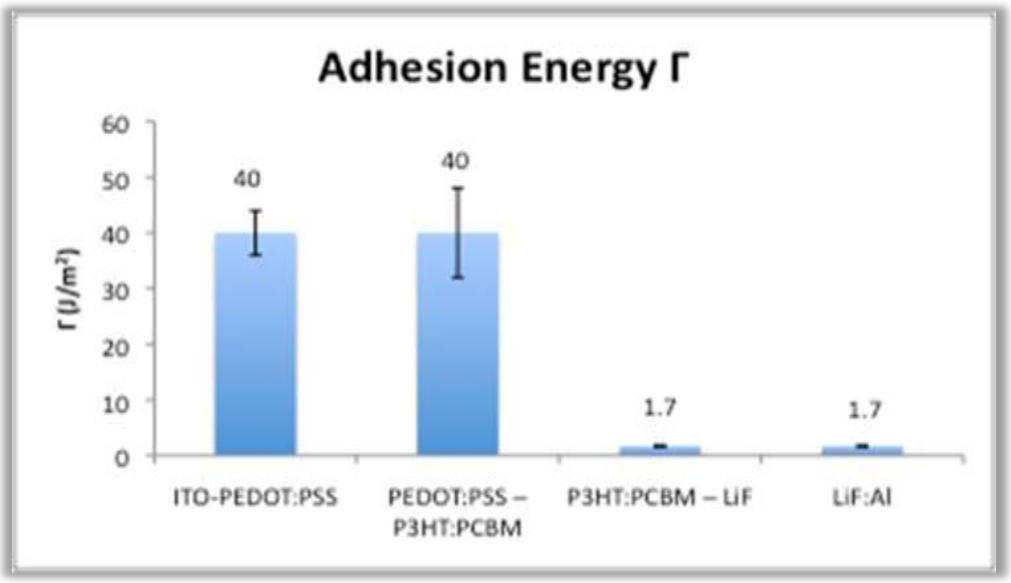

Figure 4.11 Adhesion energy for different layers in OSOLs

4.1 Results

The modeling of the contacts was done by using Matlab program *version R2007b MatWorks Inc. Massachusetts, USA (see Appendix).* The various plots for the variation in void length, Young's modulus and adhesion were obtained by using the adhesion energies obtained from prior works, and equations 21, 22 and 23. Now, using the Young's moduli of gold (Au = 79 GPa) and silver (Ag = 83 GPa) and equation (21) , a plot of void length against film thickness was obtained, as shown in Figure 4.12 for cold welded Au-Ag OLED structure. The plot shows that, increase in the dust thickness h_f leads to increase in the void length *S*; which implies a decrease in the contact length *Lc*. Short contact length affects the performance and reduces lifetime of the OLED.

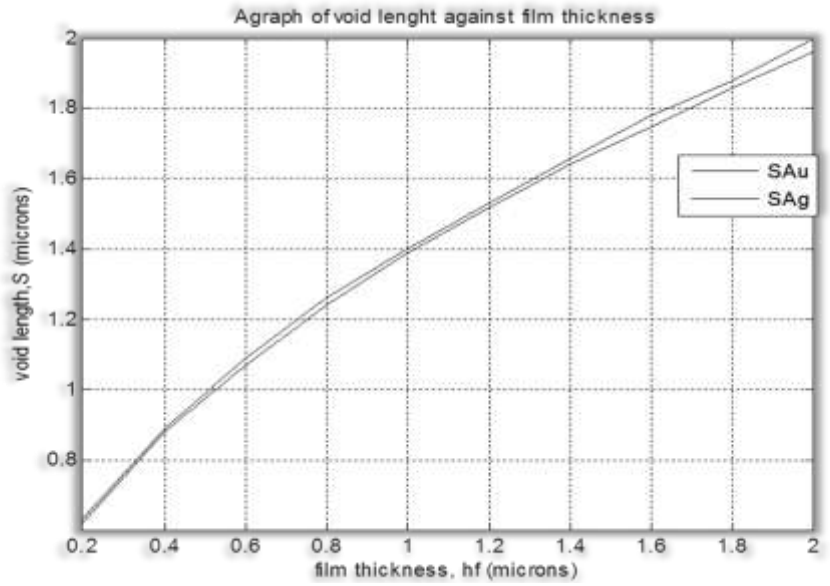

Figure 4.12 Plot of void length against film thickness of Au and Ag

Secondly, the effect of variation in adhesion energy on void length was carried out for both arc-shape and S-shape using equations (21) and (23) and the results are shown in Figure 4.13 and Figure 4.14 respectively. This plots show that, void length decreases as the adhesion between the interfaces increase for both arc-shape and S-shape void types. And at low Young's modulus, we achieve better contacts.

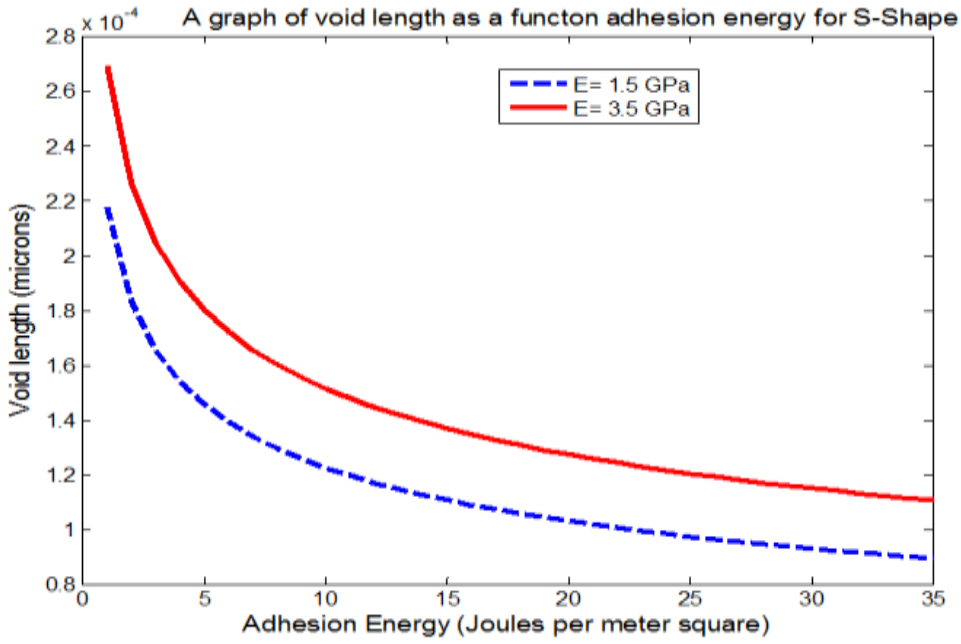

Figure 4.13 Plot of void length versus adhesion energy for S-shape

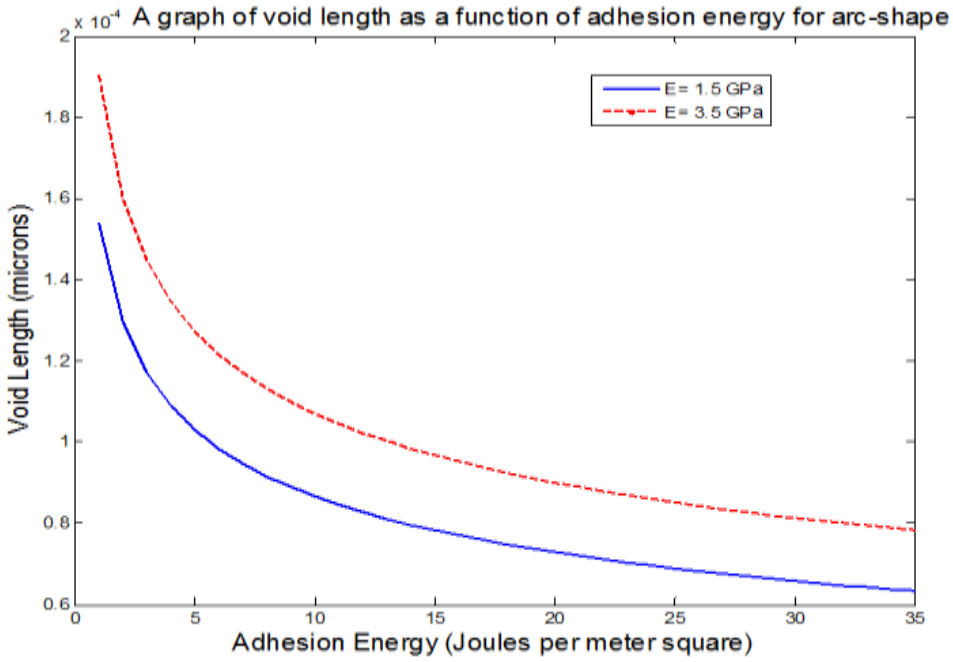

Figure 4.14 Plot of void length versus Adhesion energy for arc-shape

Thirdly, the results for the effect of variation in adhesion energy on the ratio of the contact lengths are presented in Figure 4.15 and Figure 4.16 .It can be concluded that as the adhesion between the layers increase, the ratio of the lengths, L_c/L also increases.

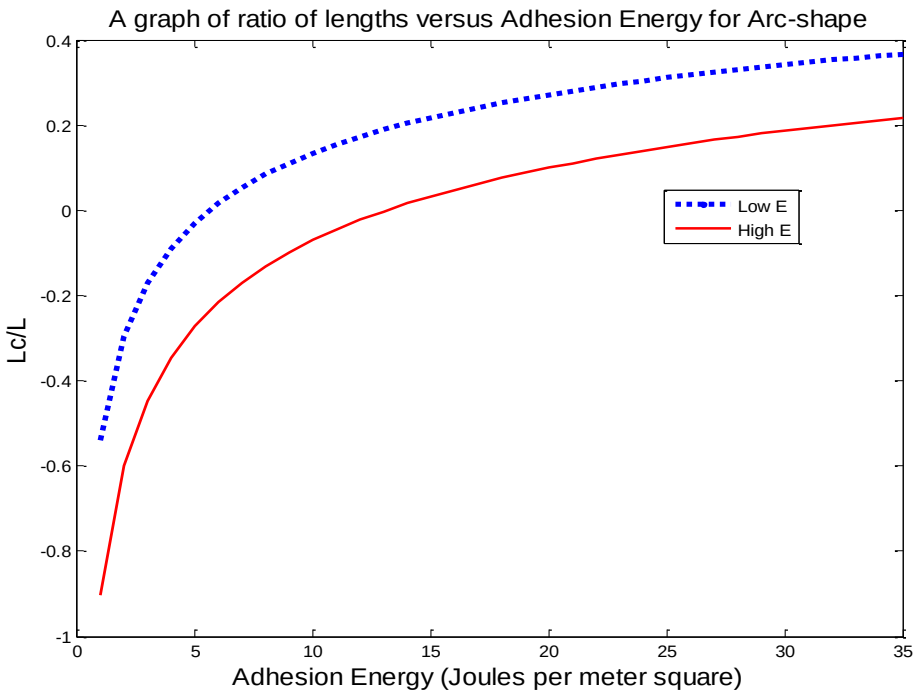

Figure 4.15 Plot of ratio of length versus adhesion energy for arc-shaped

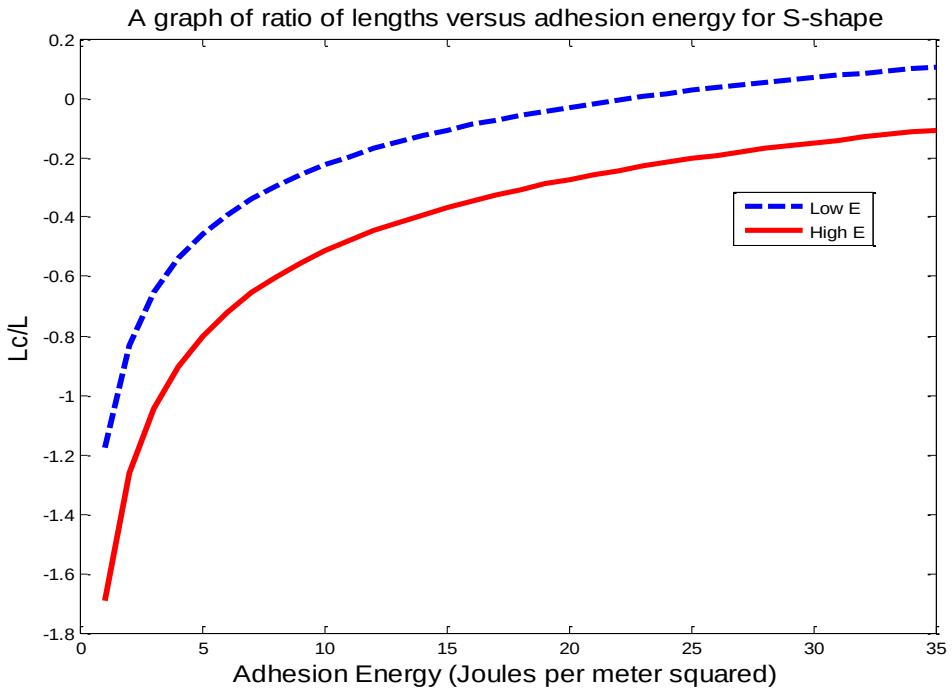

Figure 4.16 Plot of ratio of lengths versus adhesion energy for S-shape

Finally, the effect of Young's modulus of the materials on the void length was modelled and the results are shown in the plots below. Figure 4.17 shows that void length increases as the Young's modulus increase. Also as the Young's modulus increases, a decrease in the ratio of the lengths is observed, as shown in Fig. 4.18. In both cases, S-shape void type gives larger contact length than in arc-shape void type. For large applied pressure, contacts between the layered structure is small and device performance is low.

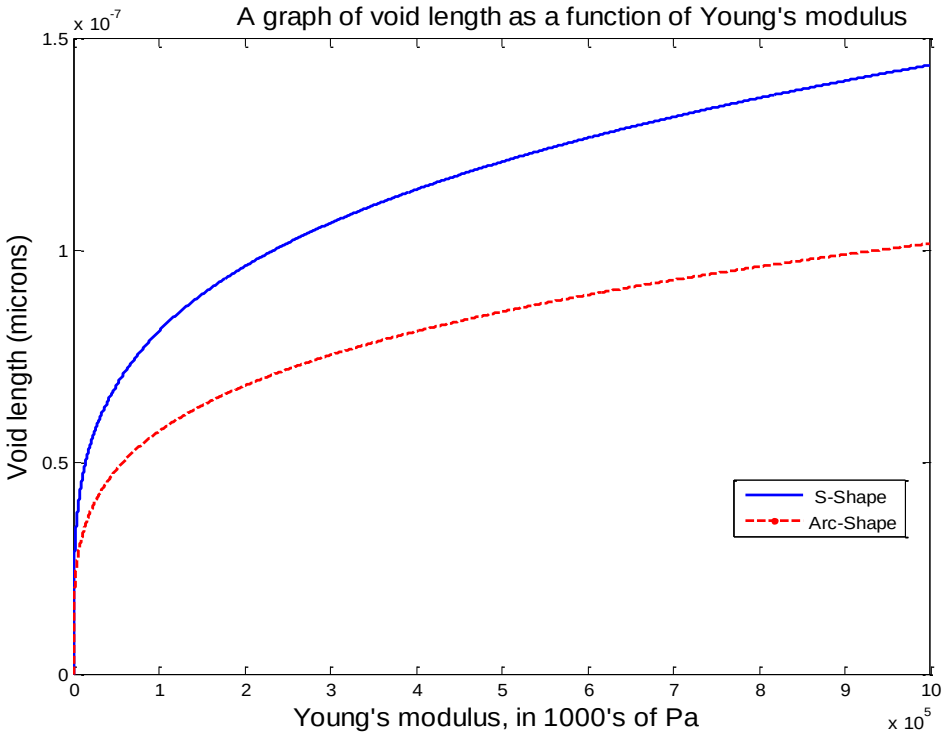

Figure 4.17 Plot of void length versus Young's modulus

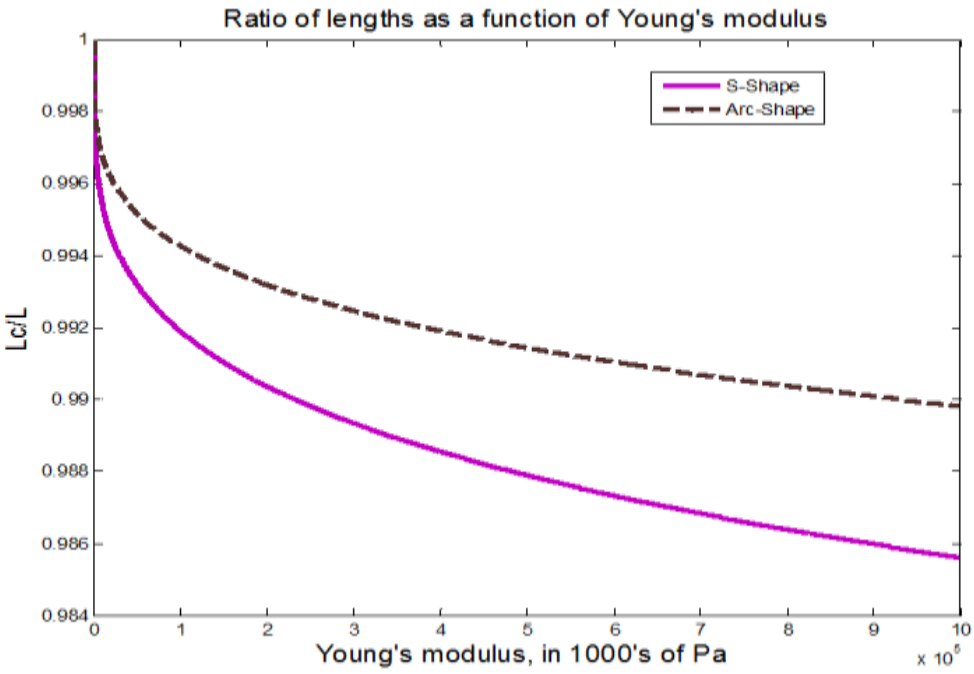

Figure 4.18 plot of ratio of lengths versus Young's modulus

4.2 Implications

The results from the modeling and plots depicts that increased adhesion promotes more intimate contact and greater contact lengths during the fabrication of organic electronic structures. Moreover, since the Young's modulus is related to force and thereby pressure, the results for the variation in Young's modulus shows that, materials with low Young's modulus gives greater contact lengths than materials with high modulus. These implications are significant for the fabrication of OLEDS and Hybrid electronic structures by cold welding or lamination processes.

The results in the prior work by Cao et al.[11], suggested that large area cold welding can be achieved at very low pressures using an elastometric soft stamp. Finite element analysis was used to model the stamping in the presence of dust particles and the results were consistent with experimental observation.

The result from this work is consistent with results obtained in work done by Akande et al.[2] and Cao et al.[11] This work reveals that low efficiencies recorded for OLEDs and HOISOLs could be due to the presence of dust particles, in the case of OLEDs, or TiO_2 nanoparticles, in HOISOLs, at the interfaces. This presence of void decreases the contact length between the active layers. Thus, moderate pressure should be applied during fabrication of these electronic devices when using cold welding or lamination technique, because excessive pressure could result in sinking in the films which deforms the layer and reduces the layer for electron flow in the structure, (Fig.3.11b).

CHAPTER FIVE

5.0 Conclusions

In this work, analytical method was developed based on the knowledge of cantilever beam and energy balance approach was employed to model the surface contact of hybrid organic/inorganic structures and OLEDs during fabrication.

The model shows that greater contact lengths and lower sink-in effects can be achieved by considering the effects of adhesion and pressure between metals. Increased adhesion can also promote more intimate contact (greater contact lengths) during fabrication processes.

Aside the presence of dust particles embedded between laminated interfaces, this work suggests that, the presence of TiO_2 nanoparticles on layered interfaces also have significant effect on the profile of adhesion and this must be considered in the design process of electronic structures in order to optimize their performance.

5.1 Future Works

This paper does not involve computational modeling due to time constraints. This would be done by Finite element analysis and compare the results. Also, experimental work could be done using lamination process technique to fabricate HOISOL or HOILED structure with/without TiO_2 (Fig 3.11) and then verify the effect of pressure on the device by varying pressure between 10-100 MPa, and finally carry out I-V characterization of the device to observe the effect of presence of TiO_2 on charge and light transport in Hybrid Organic/Inorganic Solar cells. Notwithstanding, fabrications must be done in clean semiconductor room to avoid introduction of defects on the interfaces.

References for Chapter 3 and 4

1. S. R. Forrest, Org. Electron. **4**, 45 (2003).

2. Wali O. Akande, Yifang Cao, Nan Yao & Wole Soboyejo, *Adhesion and the cold welding of gold-silver thin films.* Journal of Applied Physics **107**, 043519 (2010).

3. S. F. Lim, L. Ke, W. Wang, and S. J. Chua, Appl. Phys. Lett. **78**, 2116 (2001).

4. P. E. Burrows, V. Bulovic, S. R. Forrest, L. S. Sapochak, D. M. McCarty, and M. E. Thompson, Appl. Phys. Lett. **65**, 2922 (1994).

5. C. Kim, P. E. Burrows, and S. R. Forrest, Science **288**, 831 (2000).

6. J. W. P. Hsu, Mater. Today **8**, 42 (2005).

7. T.-W. Lee, J. Zaumseil, Z. Bao, J. W. P. Hsu, and J. A. Rogers, Proc. Natl.Acad. Sci. U.S.A. **101**, 429 (2004).

8. T.Tong, B. Babatope, S Admassie, J. Meng, O. Akwogu, W. Akande, and W. O. Soboyejo, *Adhesion in organic electronic structures*, J. of Appl. Phys. **106**. 083708 (2009).

9. W. Akande, *Interfacial Reliability and Failure Mechanisms in Organic Light Emitting Diodes,* PhD Thesis, Princeton Univerisy, September 2010.

10. Z. Zong, Y. Cao, N. Rahbar, and W. O. Soboyejo, *Nano- and microscale adhesion energy measurement for Au-Au contacts in microswitch structures*, Journal of Applied Physics, 100, 104313 (2006).

11. Yifang Cao et al. *Effects of dust particles and layer properties on organic electronic devices fabricated by stamping*, Journal of Applied Physics 98, 033713 (2005).

12. A. C. Fischer-Cripps, f*irst Edition, Mechanical Engineering Series,* Springer-Verlag, New York, 2000.

13. B. V. Derjaguin, V. M. Muller, and Y. P. Toporov, *Progress in Surface Science* 45, 131-143 (1994).

14. K. L. Johnson, K. Kendall, and A. D. Roberts, *Proceedings of the Royal Society of London. Series A, Mathematical and Physical Sciences* 324, 301-313 (1971).

15. *D.* Maugis, *Journal of Colloid and Interface Science* 150, 243-269 (1992).

16. R.W Carpwick, & D.F. Ogletree, *Colloid interface science* 211, 395 (1999).

17. O. Pietrement & M. Troyon, *Colloid interface Science*. 226, 166 (200).

18. H. Hertz, *J.* Reine Angew. *Math*. 92, 156 (1881).

19. Jong H. Kim, Soon-min Seo, and Hong H. Lee, *Nanovoid nature and compression effects in organic light emitting diode*, Appl. Phys. Lett. 90, 143521 (2007).

Appendix

A: Matlab code for the modeling of the void length and adhesion energy.

```
 Clear all, close all
%%%%%%%%%%%%%%%%%%%%%%%%%%%%%%%%%%%%%%%%%%%%%%%%%%
%%%%%%%%%%%%%%%%%  Void and adhesion simulation  %%%%%%%%%%%%%
%%%%%%%%%%%%%%%%%%%%%%%%%%%%%%%%%%%%%%%%%%%%%%%%%%

E1=3.5*10^9;               % Young's modulus
t=1.00*10^-4;              % Thickness
w=5*10^-5;                 % Breadth
I=(w*t^3)/12;              % Second moment of area
h=1*10^-6;                 % Void's height
E=1.5*10^9;                % Young's modulus
l=10^-4;                   % Length
b=((3/2)*E*t^3*h^2);       % Constant for s-shape (E)
b1=((3/2)*E1*t^3*h^2);     % Constant for s-shape (E1)
b3=((3/8)*E*t^3*h^2);      % constant for arc-shape (E)
b4=((3/8)*E1*t^3*h^2);     % constant for arc-shape (E1)
j=0:1:35;                  % variation of adhesion energy
k=35;
s=zeros(1,size(j,2));
s1=zeros(1,size(j,2));
s3=zeros(1,size(j,2));
s4=zeros(1,size(j,2));

for n=1:size(j,2);
    s(n)=[b*j(n)^-1]^(1/4);    % Void length for the s-shape (E)
    s1(n)=[b1*j(n)^-1]^(1/4); % Void length for the s-shape(E1)
    s3(n)=[b3*j(n)^-1]^(1/4);%Void length for the arc-shape (E)
    s4(n)=[b4*j(n)^-1]^(1/4);%Void length for the arc-shape(E1)

end
lc=l-s;                   % Contact length for the s-shape (E)
lc1=l-s1;
lc3=l-s3;                 % Contact length for the arc-shape (E)
lc4=l-s4;
z=lc/l;                   % Ratio of lc/l for the s-shape (E)
z1=lc1/l;
z3=lc3/l;                 % Ratio of lc/l for the arc-shape (E)
z4=lc4/l;

plot(j,s,'b-'); hold on
plot(j,s1,'r-'); hold on
%plot(j,s3,'b-'); hold on
%plot(j,s4,'r-'); hold on
%plot(j,z,'b-'); hold on
%plot(j,z1,'r-'); hold on
%plot(j,z3,'b-'); hold on
%plot(j,z4,'r-'); hold on
```

B: Matlab code for variation of Young's modulus.

```
%%%%%% Program for variation of Young's modulus%%%%%%%%%%%%%

            t=1.00*10^-6;                   % Metal's thickness
            h=1*10^-7;                      % Void height
            j= 35;                          % Adhesion energy
            l=1*10^-5;                      % Length
            b=((3/2)*t^3*h^2);              % Constant for s-shape
            b1=((3/8)*t^3*h^2);             % Constant for arc-shape
            e=0:100:10^6;                   %  variation Young's modulus
            s=zeros(1,size(e,2));
            s1=zeros(1,size(e,2));
            for n=1:size(e,2);
                s(n)=[b*e(n)*j^-1]^(1/4);   % Void length for the s-shape
                s1(n)=[b1*e(n)*j^-1]^(1/4); % Void length for the arc-shape
            end
            lc=l-s;                       % Contact length for the s-shape
            lc1=l-s1;                     % Contact length for the arc-shape
            z=lc/l;                       % Ratio of lc/l for the s-shape
            z1=lc1/l;                     % Ratio of lc/l for the arc-shape

            %plot(e,s,'b-'); hold on
            %plot(e,s1,'r-'); hold on
            plot(e,z,'b-'); hold on
            plot(e,z1,'r-'); hold on
```